

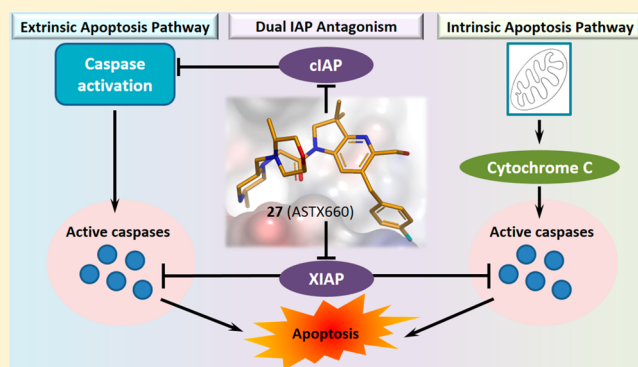
# A Fragment-Derived Clinical Candidate for Antagonism of X-Linked and Cellular Inhibitor of Apoptosis Proteins: 1-(6-[(4-Fluorophenyl)methyl]-5-(hydroxymethyl)-3,3-dimethyl-1*H*,2*H*,3*H*-pyrrolo[3,2-*b*]pyridin-1-yl)-2-[(2*R*,5*R*)-5-methyl-2-[(3*R*)-3-methylmorpholin-4-yl]methyl]piperazin-1-yl]ethan-1-one (ASTX660)

Christopher N. Johnson,\*<sup>1</sup> Jong Sook Ahn, Ildiko M. Buck, Elisabetta Chiarparin, James E. H. Day, Anna Hopkins, Steven Howard, Edward J. Lewis, Vanessa Martins, Alessia Millemaggi, Joanne M. Munck, Lee W. Page, Torren Peakman, Michael Reader, Sharna J. Rich, Gordon Saxty, Tomoko Smyth, Neil T. Thompson, George A. Ward, Pamela A. Williams, Nicola E. Wilsher, and Gianni Chessari

Astex Pharmaceuticals, 436 Cambridge Science Park, Milton Road, Cambridge CB4 0QA, United Kingdom

## Supporting Information

**ABSTRACT:** Inhibitor of apoptosis proteins (IAPs) are promising anticancer targets, given their roles in the evasion of apoptosis. Several peptidomimetic IAP antagonists, with inherent selectivity for cellular IAP (cIAP) over X-linked IAP (XIAP), have been tested in the clinic. A fragment screening approach followed by structure-based optimization has previously been reported that resulted in a low-nanomolar cIAP1 and XIAP antagonist lead molecule with a more balanced cIAP–XIAP profile. We now report the further structure-guided optimization of the lead, with a view to improving the metabolic stability and cardiac safety profile, to give the nonpeptidomimetic antagonist clinical candidate 27 (ASTX660), currently being tested in a phase 1/2 clinical trial (NCT02503423).



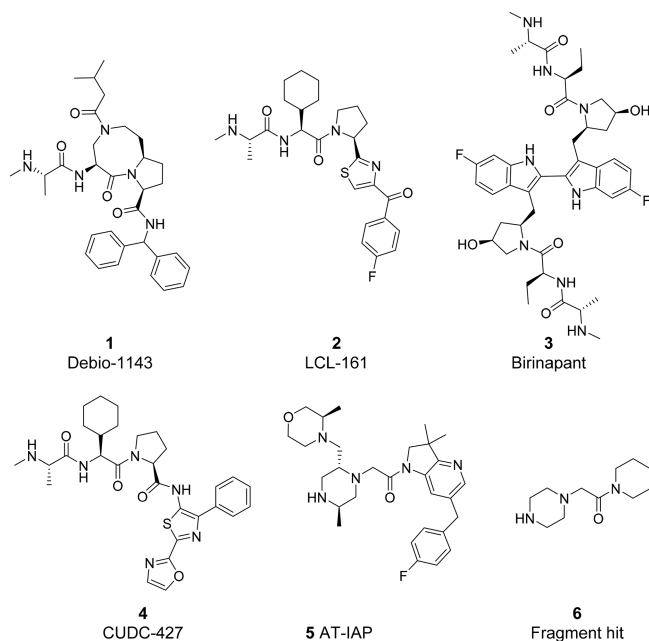
## INTRODUCTION

One of the hallmarks of cancer is evasion of apoptosis,<sup>1</sup> achievable through overexpression of antiapoptotic proteins. Inhibitor of apoptosis proteins (IAPs), such as cellular IAP1 and 2 (cIAP1 and cIAP2 respectively) and X-linked IAP (XIAP), are key regulators of antiapoptotic and pro-survival signaling. XIAP directly inhibits caspases, cysteine proteases with an essential role in the apoptotic cascade. In contrast, cIAPs prevent the formation of pro-apoptotic signaling complexes such as complex-II, composed of Fas-associated protein with death domain (FADD), procaspase-8, and receptor-interacting serine/threonine-protein kinase 1 (RIPK1). These effects cause suppression of apoptosis through both extrinsic and intrinsic apoptosis pathways.<sup>2–4</sup> IAP dysregulation occurs in various cancers and is associated with tumor growth and poor prognosis, rendering IAPs attractive targets for anticancer therapy.<sup>5</sup> IAPs are characterized by one or more baculovirus IAP repeat (BIR) domains which mediate protein–protein interactions. Some family members (e.g., cIAP and XIAP) also possess Really Interesting New Gene (RING) zinc finger domains with E3 ubiquitin ligase activity.<sup>6,7</sup> XIAP

antiapoptotic activity is mediated by direct binding to and inactivation of caspases via BIR domains.<sup>8</sup> IAP antagonists such as the endogenous second mitochondria derived activator of caspases (SMAC) bind competitively to IAP BIR domains, thus disrupting interactions such as those between XIAP and caspase 9.<sup>9</sup> On binding to cIAP1 and cIAP2, SMAC activates E3 ligase function leading to autoubiquitination and proteasomal degradation.<sup>10</sup> Loss of cIAP, together with the release of the XIAP-mediated caspase block, leads to a sustained pro-apoptotic effect in the presence of TNF- $\alpha$  via the extrinsic apoptosis pathway. Hence, tumors with sufficient levels of TNF- $\alpha$  in their environment may be highly susceptible to IAP antagonism.<sup>11</sup> Furthermore, antagonism of the XIAP-mediated caspase block promotes apoptosis induced by stimulation of the intrinsic apoptosis pathway by agents such as chemotherapeutics or DNA damaging agents.<sup>12</sup> A cIAP/XIAP antagonist might therefore be used to enhance apoptosis through both extrinsic and intrinsic pathways.

Received: June 6, 2018

Previously, IAPs have been targeted by antisense oligonucleotides and antagonist small molecules.<sup>4</sup> Pioneering research has led to first generation SMAC-mimetic IAP antagonists such as 1–4, with designs based on AVPI, the N-terminal sequence of SMAC, and these have shown promising preclinical activity.<sup>13–16</sup> However, all of these compounds are selective for cIAP.



We previously reported a fragment-based drug design (FBDD) approach to the discovery of a nonpeptidomimetic, low nanomolar, orally bioavailable antagonist of cIAP1 and XIAP, designated AT-IAP 5,<sup>17,18</sup> starting from the millimolar-affinity fragment 6. Compound 5 had particularly high affinity for XIAP and a more balanced cIAP1/XIAP profile (~16-fold) compared to AVPI-based antagonists 1–4, where selectivity for cIAP1 versus XIAP ranged from 39- to 227-fold.<sup>18,19</sup> This selectivity observation was structurally well understood in terms of the interactions made between cIAP1 or XIAP and the piperazine moiety of 5, compared with those made by the terminal N-methylated alanine of the first generation peptidomimetic compounds. Here we describe further medicinal chemistry optimization of advanced lead 5 to give ASTX660 27,<sup>19</sup> which is now being evaluated in a phase 1/2 clinical trial in cancer patients.

## RESULTS AND DISCUSSION

Advanced lead 5 was a useful chemical probe, having oral bioavailability in the mouse (22%) and antitumor growth activity in mouse MDA-MB-231 and A375 xenograft models.<sup>18</sup> The compound also had moderate plasma clearance (26 mL min<sup>-1</sup> kg<sup>-1</sup>) and oral bioavailability in the rat (24%) (see Table 1). It was important to characterize the pharmacokinetic (PK) profile in a nonrodent species, in consideration of the need to perform toxicological evaluation on the compound as a potential drug candidate. It has been previously reported that dogs are very sensitive to NF-κB pathway effects caused by antagonism of cIAP1,<sup>20</sup> and therefore a nonhuman primate (NHP) may be a more appropriate nonrodent species for toxicology studies. We therefore determined the PK profile of 5 in cynomolgus monkey (Table 1) via the oral and intravenous route. Plasma clearance was moderate (<50%

**Table 1. Cross-Species Pharmacokinetic Parameters for Compound 5**

species <sup>a</sup>	CL <sub>p</sub> mL min <sup>-1</sup> kg <sup>-1</sup>	V <sub>ss</sub> L kg <sup>-1</sup>	C <sub>max</sub> (PO) ng mL <sup>-1</sup>	F%
mouse	41	6.4	120	22
rat	26	12	47	24
cynomolgus monkey	17	3.7	22	2

<sup>a</sup>Plasma clearance (CL<sub>p</sub>), volume of distribution at steady state (V<sub>ss</sub>), maximum concentration in plasma (C<sub>max</sub>) and oral bioavailability (F) were determined for each species using an intravenous (IV) dose of 1 mg/kg and an oral (PO) dose of 5 mg/kg. For assay details see Experimental Section.

liver blood flow), but oral bioavailability at 5 mg/kg was only 2%. The low oral bioavailability in NHP indicated a potential for suboptimal exposure in humans. Furthermore, the low peak concentration obtained in plasma (C<sub>max</sub>) suggested that a key goal would be to obtain a compound capable of attaining plasma drug levels in the NHP species equivalent to or greater than those producing a pharmacodynamic response in mouse.<sup>18</sup> In addition, compound 5 was assessed for potential cardiac toxicity in a I<sub>Kr</sub> potassium channel (hERG) population patch clamp (PPC) assay, and it showed inhibition with IC<sub>50</sub> 9 μM. Therefore, a further round of optimization was undertaken starting from 5, with the objective of improving PK profile in the NHP and reducing hERG inhibition.

In order to understand the oral exposure in cynomolgus monkey, the permeability and efflux potential of 5 were evaluated in a Caco2 monolayer assay (efflux ratio A-B/B-A = 36 and permeability = 1.1 × 10<sup>-6</sup> cm s<sup>-1</sup>), suggesting that metabolism may explain the *in vivo* observations better than permeability. Compound 5 had significant *in vitro* intrinsic clearance in microsomes and hepatocytes across species, with the exception of rat (Supporting Information Table S2), and the low stability in monkey microsomes was notable. Compound 5 also showed significant *in vivo* clearance across species, so the route of metabolism was investigated in mouse, rat, NHP and human liver hepatocytes (Figure 1). Assuming the mass spectrometric response of the parent compound and proposed metabolites is similar, the main metabolic route was identified as the opening of the morpholine ring to give metabolite M1 (<7% response compared to parent in mouse and human, 20% compared to parent in NHP), followed by conversion to the primary amine derivative (metabolite M2). Piperazine ring-opened amine M4 was identified as a minor metabolite (<1% compared to parent in mouse and human, 4% compared to parent in NHP). A further minor oxidation metabolite M3 of compound 5 was identified in mouse, NHP and human hepatocytes, though the site of oxidation was not elucidated. No metabolites were observed in rat hepatocyte preparations due to the low metabolic turnover of 5 in this system.

Cytochrome P450 (CYP) phenotyping was also carried out in human supersomes in order to determine the enzymes primarily responsible for compound turnover. Importantly, the observed metabolism was found to be mediated by CYP3A4. Cynomolgus monkeys are known to highly express CYP3A8 in the gut,<sup>21</sup> which can lead to low exposure of compounds metabolized by CYP3A enzymes. We therefore hypothesized that extensive gut metabolism in NHP was an important contributor to the low oral bioavailability of 5 in this species,

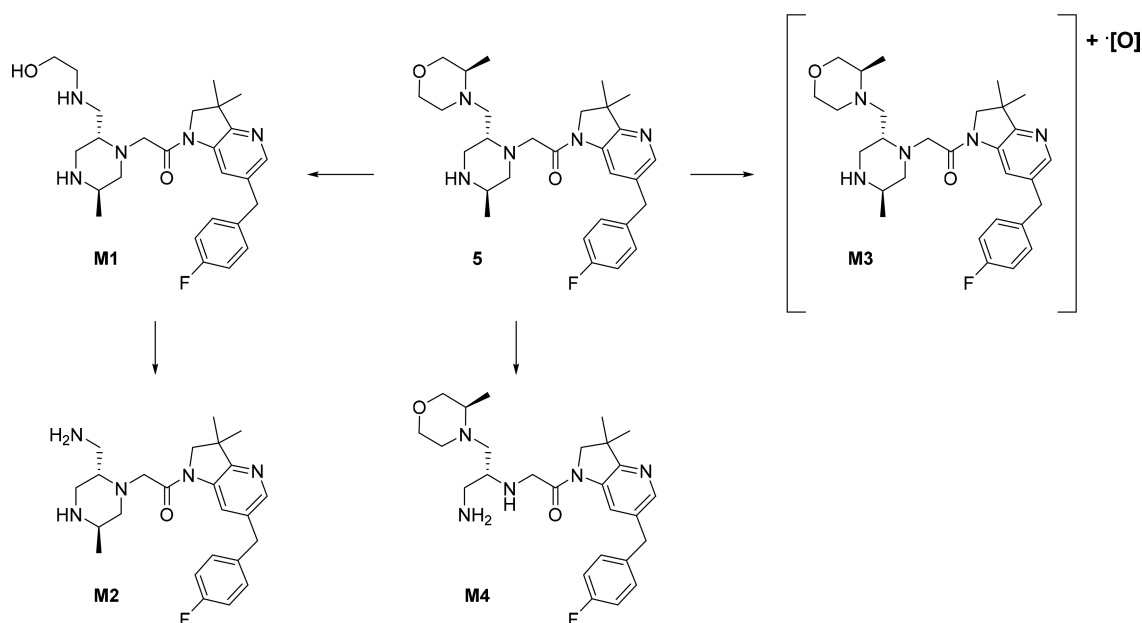


**Figure 1.** Proposed route of metabolism of compound 5 in mouse, NHP, and human hepatocytes.

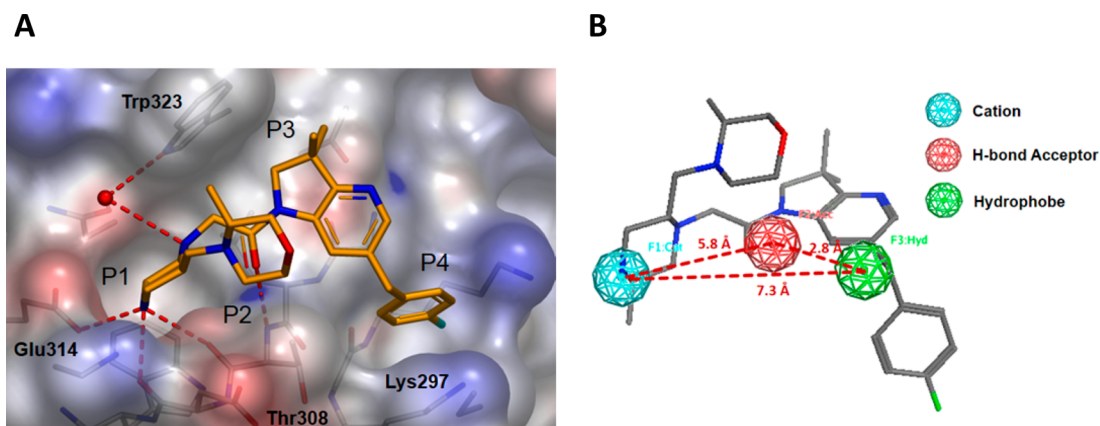


**Figure 2.** (A) X-ray crystal structure of compound 5 (PDB code 5M6L) bound to XIAP with pockets P1–P4 labeled. Connolly surface of protein is colored by electrostatic potential (blue = positive, red = negative), hydrogen bonds are displayed as dashed red lines, and crystallographic water is shown as a red sphere. (B) Aronov hERG pharmacophore overlaid on bound conformation of compound 5. Pharmacophore points are shown as color-coded mesh spheres according to the legend, with distances between features marked by dashed red lines.

and thus incorporated a CYP3A4 turnover assay into the screening cascade for lead optimization.

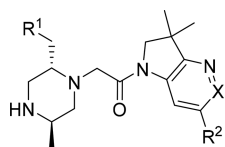
To assess hERG activity, we screened using the PPC assay<sup>22</sup> to identify compounds with lower risk of QT interval prolongation in vivo. We assessed percentage inhibition at three concentrations (10, 30, and 100  $\mu\text{M}$ ) and determined PPC  $\text{IC}_{50}$  values for key compounds of interest. For simplicity, the subsequent data tables show only data obtained at 30  $\mu\text{M}$ ; compound 5 itself gave 70% inhibition at 30  $\mu\text{M}$ .

During the fragment to lead campaign that led to compound 5, crystal structures had been used primarily to drive potency increases by growing efficiently into pockets. However, the principal objectives were now different: to improve the metabolism and cardiac profile. Structural understanding was nonetheless essential in identifying parts of the molecule where changes might be tolerated as opposed to those that would likely result in potential reduction of binding affinity. For example, the piperazine amide core of 5 is known to make several important polar interactions to the protein as well as

filling the P1 pocket (Figure 2A), so the optimization strategy required that this part of the molecule should not be changed. Examination of the binding mode shows that the metabolically labile methylmorpholine group occupies the P2 pocket and that space exists for further variation in this part of the molecule. The azaindoline bicycle stacks on a flat part of the protein and also occupies P3 by virtue of the gem-dimethyl substitution, while the fluorobenzyl fills P4. The structure suggests that there may be a limited scope for increasing the size of the P4 substituent, but that some modifications may be tolerated in the bicycle, subject to satisfying the previously described requirement to match the electrostatic potential of the aryl portion to the presence of an electronegative patch on the protein surface.<sup>17</sup>

In order to attenuate the hERG activity, we considered how compound 5 might map to a number of proposed hERG pharmacophore models. In the model proposed by Aronov,<sup>23</sup> a number of known hERG ligands have an H-bond acceptor positioned between positively charged nitrogen and hydro-

Table 2. Initial SAR Exploration around Compound 5



Cpd	R <sup>1</sup>	X	R <sup>2</sup>	Cellular IC <sub>50</sub> (nM)			CYP3A4 t <sub>1/2</sub> (min)	hERG PPC (%inh. at 30 μM)
				XIAP <sup>a</sup>	cIAP1 <sup>b</sup>	MDA- MB-231 <sup>c</sup>		
5		CH	CH <sub>2</sub> Ph-(4-F)	5.1	0.32	4.4	13	70
7		CH	CH <sub>2</sub> Ph-(4-F)	20	4.2	26	NT <sup>d</sup>	NT
8		CH	CH <sub>2</sub> Ph-(4-F)	2.9	0.19	1.2	5.9	71
9		CH	CH <sub>2</sub> Ph-(4-F)	14	0.62	7.0	NT	NT
10		CH	CH <sub>2</sub> Ph-(4-F)	14	6.5	22	40	36
11		CH	CH <sub>2</sub> Ph-(4-F)	18	3.8	14	32	49
12		CH	CH <sub>2</sub> Ph-(4-F)	30	1.3	8.3	45	58
13		N	CH <sub>2</sub> Ph-(4-F)	47	2.5	16	38	12
14		N	CH <sub>2</sub> Ph-(2,4-diF)	12	0.34	5.4	>70	27

<sup>a</sup>Cellular XIAP-caspase 9 immunoprecipitation assay. <sup>b</sup>Intracellular degradation of cIAP1 in MDA-MB-231 cells. <sup>c</sup>MDA-MB-231 cell proliferation assay (cIAP1 sensitive). <sup>d</sup>Not tested. For all assay details see [Experimental Section](#).

phobic centroid. The three-dimensional structure of **5** in its bound conformation ([Figure 2B](#)) has all three elements in a similar geometric relationship. Our design strategy then considered how one or more of these pharmacophore elements could be perturbed in order to attenuate binding to hERG. The binding mode of **5** in XIAP ([Figure 2A](#)) suggests that judicious placement of polarity in the region of the hydrophobic centroid could be a viable option to decrease hERG channel inhibition while retaining target potency.

We thus had two design goals: the first was to reduce metabolism by making changes to the P2 morpholine moiety, and the second was to introduce polarity in the region of the P4 group and azaindoline heterobicyclic. [Table 2](#) shows modifications to the P2 group aimed at improving metabolic stability. The effect of these changes on cellular XIAP and cIAP1 potency, together with antiproliferative effect in the MDA-MB-231 cell line (sensitive to cIAP1 inhibition) is shown, alongside compound half-life on incubation with CYP3A4 supersomes, together with hERG PPC inhibition data. Cell-based assays for cIAP1 and XIAP were as previously reported:<sup>18</sup> for XIAP, a XIAP-caspase 9 immunoprecipitation (IP) assay was used in a HEK293 cell line overexpressing XIAP and caspase 9, while for the cIAP1 assay, intracellular cIAP1 degradation in MDA-MB-231 cells was measured as a surrogate for cIAP1 affinity.

Examination of the P2 pocket environment in the X-ray crystal structure of **5** bound to XIAP indicated that attempts to block metabolism in the morpholine ring by adding increased steric bulk should be tolerated in terms of binding affinity. Therefore morpholine derivatives bearing additional methyl substituents were synthesized **7–9**. Of these, **8** had exceptional potency at both XIAP and cIAP1 and had improved potency in the MDA-MB-231 cell proliferation assay compared to **5**. Previously, promising activity had been seen with a P2 2-pyrrolidinone substituent,<sup>18</sup> where a folded conformation necessary for binding was favored by the complementary electrostatic potentials of the amide region of the piperazine-azaindoline scaffold and the lactam carbonyl. We therefore introduced a carbonyl into the morpholine group to give **10**. Although this compound had relatively modest XIAP potency and MDA-MB-231 antiproliferative activity, both CYP3A4 turnover and hERG activity were reduced. Further exploration of lactams was undertaken, aiming to fill additional space in the P2 region while continuing to favor a folded conformation. It was thought that extending the  $\pi$ -system of the lactam carbonyl might promote hydrophobic collapse-induced folding, so the unsaturated lactam **11** and benzolactam **12** were prepared. Both had improved CYP3A4 stability compared to **5**, but the effect on hERG was marginal. Benzolactam **12** indeed adopted the desired folded conformation in the XIAP X-ray

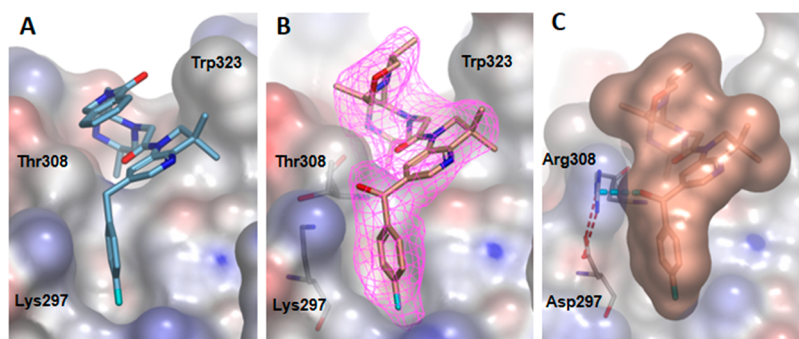


**Figure 3.** (A) X-ray crystal structure of benzolactam **12** bound to XIAP. (B) X-ray crystal structure of compound **21** bound to XIAP with ligand electron density map ( $F_o - F_c$  maps contoured at  $1\sigma$  and clipped around the ligand) shown as magenta mesh. (C) Protein structure of cIAP1 overlaid with XIAP – compound **21** complex in same frame of reference. For clarity, XIAP protein is not displayed. The salt bridge between Arg308 and Asp297 is shown as a dashed cyan line. For (A), (B), and (C), the displayed protein Connolly surface is colored by electrostatic potential (blue = positive, red = negative).

crystal structure (Figure 3A), but target potency was slightly decreased. However, we reasoned that the benzolactam P2 moiety might offer an opportunity to introduce a group capable of disrupting the hERG pharmacophore, especially if it could be established that a folded conformation predominates in solution. In the  $^1\text{H}$  NMR spectrum of **12** in  $\text{CD}_3\text{OD}$ , the chemical shifts of the methyl groups on the azaindoline 5-membered ring were significantly different (3H,  $\delta$ 1.34 and 3H,  $\delta$ 1.48), suggesting a perturbation of one resonance due to proximity of an aromatic group. Such a situation could arise if the benzolactam group was folded in the manner previously seen for the simple pyrrolidinone and the morpholine of compound **5**. NMR spectroscopy on **12** dissolved in 50 mM pH 7.4 phosphate buffer confirmed that observations in solution are consistent with the X-ray conformation (see Supporting Information, Figure S1).

Having identified a bicyclic P2 substituent of potential interest, we investigated the effect of adding an additional nitrogen to the azaindoline moiety as a means of disrupting the hERG pharmacophore. Diazaindoline **13** encouragingly had good CYP3A4 stability and reduced hERG inhibition, and replacement of the P4 4-fluorobenzyl with 2,4-difluorobenzyl **14** restored good target potency without significant detriment to the CYP3A4 and hERG profile. The PK profile of compound **14** was characterized in mouse and cynomolgus monkey. Oral bioavailability in mouse was low (2% at 10 mg/kg), but in monkey was significantly improved compared with original lead **5** (18% at 5 mg/kg). In the PPC hERG assay, **14** had low inhibition at 30  $\mu\text{M}$ , suggesting an improved cardiac profile and respectable exposure in NHP were achievable concurrently within the overall chemotype. Nevertheless, further optimization was required in order to address the low oral exposure in mouse and the relatively unbalanced IAP antagonism profile of **14** (>30 fold selectivity for cIAP1 over XIAP) compared to lead compound **5**.

At this stage of the optimization, a total of 53 compounds had been analyzed for hERG and 32 compounds for CYP3A4. With respect to physicochemical properties, a broad trend could be observed with respect to C logP, where highly lipophilic compounds had the least favorable profiles. However, the overall correlation was weak, and it was difficult to set a target value for C logP that could usefully guide further optimization. Metabolic stability and hERG inhibitory liability are often influenced by lipophilicity,<sup>24</sup> and therefore we were keen to identify an alternative lipophilicity measure that would

guide the optimization more effectively. Chromatographic logD (ChrlogD) measurements were therefore performed at pH 7.4 on the same compound set (see Experimental Section), and the results were plotted against hERG inhibition in the PPC assay and half-life in the CYP3A4 turnover assay (Figure 4, panels A and B respectively). Here the correlation was much

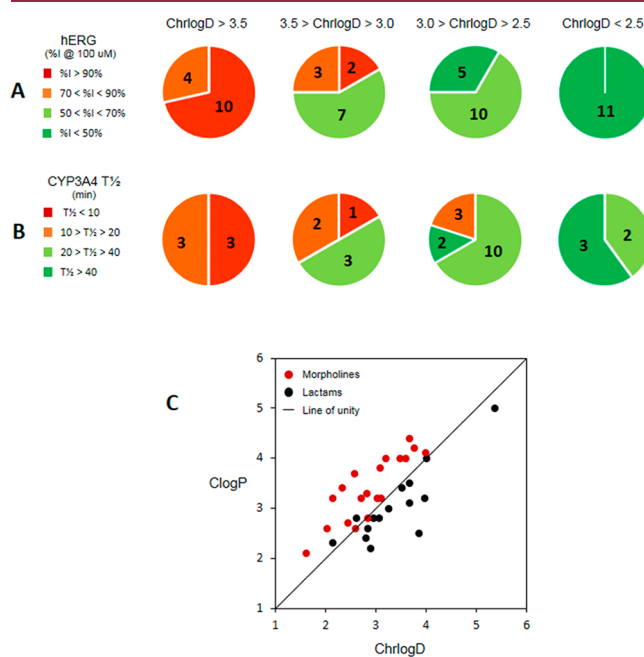
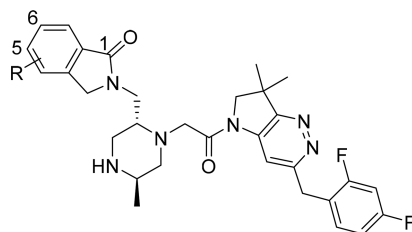


**Figure 4.** (A) Percentage hERG inhibition at 100  $\mu\text{M}$  in the population patch clamp (PPC) assay plotted for different ranges of chromatographic logD (ChrlogD). Total numbers of compounds per inhibition category are displayed in each segment. (B) Half-life ( $T_{1/2}$ ) in the CYP3A4 turnover assay plotted for the same ChrlogD ranges, with total numbers per  $T_{1/2}$  category displayed in each segment (C). Scatter plot of C logP versus ChrlogD colored by P2 side chain subtype.

improved and, for both hERG inhibition and CYP3A4 stability, the data suggested that compounds with ChrlogD  $\leq 3$  should be targeted in order to maximize the chance of success. In comparison, compound **5** had a ChrlogD value of 3.7. Figure 4C shows the relationship between C logP and ChrlogD for compounds bearing morpholine and lactam P2 side chains. It can be seen that morpholine containing compounds cluster to

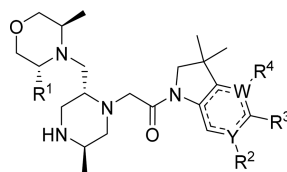
Table 3. Benzolactam Subseries SAR



Cpd	R	ChrlgD <sup>a</sup>	cellular IC <sub>50</sub> (nM)			CYP3A4 t <sub>1/2</sub> (min)	hERG PPC (%inh. at 30 μM)
			XIAP <sup>b</sup>	cIAP1 <sup>c</sup>	MDA-MB-231 <sup>d</sup>		
14	H	2.4	12	0.34	5.4	>70	27
15	4-F	2.7	4.3	0.17	0.59	>70	28
16	5-F	2.6	3.5	0.20	1.9	37	25
17	6-F	3.1	7.5	0.74	2.9	41	18
18	5-CN	3.0	16	1.0	5.2	42	19
19	6-CN	2.9	5.8	1.6	14	34	18

<sup>a</sup>Chromatographic LogD measured at pH 7.4. <sup>b</sup>Cellular XIAP-caspase 9 immunoprecipitation assay. <sup>c</sup>Intracellular degradation of cIAP1 in MDA-MB-231 cells. <sup>d</sup>MDA-MB-231 cell proliferation assay (cIAP1 sensitive). For all assay details see [Experimental Section](#).

Table 4. Morpholine Subseries SAR



Cpd	R <sup>1</sup>	R <sup>2</sup>	R <sup>3</sup>	R <sup>4</sup>	W	Y	ChrlgD <sup>a</sup>	Cellular IC <sub>50</sub> (nM)			CYP3A4 t <sub>1/2</sub> (min)	hERG PPC (%inh. at 30 μM)
								XIAP <sup>b</sup>	cIAP1 <sup>c</sup>	MDA-MB-231 <sup>d</sup>		
8	Me	CH <sub>2</sub> Ph-(4-F)	H	-	N	C	4.0	2.9	0.19	1.2	5.9	71
20	Me		H	-	N	C	NT <sup>e</sup>	47	2.3	7.9	NT	10
21	Me		H	-	N	C	2.9	7.4	3.5	15	28	7
22	Me	CH <sub>2</sub> Ph-(2-OH, 4-F)	H	-	N	C	NT	17	0.59	11	NT	NT
23	Me	CH <sub>2</sub> Ph-(4-F)	(=O)	H	N	C	2.7	5.4	0.13	2.1	39	22
24	Me	CH <sub>2</sub> Ph-(4-F)	(=O)	Me	N	C	3.2	0.83	0.18	2.4	18	14
25	Me	CH <sub>2</sub> Ph-(4-F)	(=O)	H	C	N	2.4	14	0.70	18	30	15
26	Me	CH <sub>2</sub> Ph-(4-F)	CH <sub>2</sub> OH	-	N	C	3.5	1.6	0.10	1.8	16	51
27	H	CH <sub>2</sub> Ph-(4-F)	CH <sub>2</sub> OH	-	N	C	3.1	2.8	0.22	1.8	32	30

<sup>a</sup>Chromatographic LogD measured at pH 7.4. <sup>b</sup>Cellular XIAP-caspase 9 immunoprecipitation assay. <sup>c</sup>Intracellular degradation of cIAP1 in MDA-MB-231 cells. <sup>d</sup>MDA-MB-231 cell proliferation assay (cIAP1 sensitive). <sup>e</sup>Not tested. For all assay details see [Experimental Section](#).

the left of the line of unity, whereas the lactams predominately cluster to the right. In general, the morpholines are less lipophilic than expected from the C logP value, possibly due to partial protonation of the morpholine moiety, whereas the lactams are more lipophilic than C logP would suggest.

Subsequent optimization focused on the P2 benzolactam and P2 morpholine subseries. For the benzolactams, the challenge was to identify changes that improved XIAP affinity while preserving the favorable CYP3A4 and hERG profiles. Conversely, the morpholine subseries already had excellent

XIAP and cIAP1 profiles, so we adopted the strategy of addition of polar functionality in order to ascertain whether the morpholine ring metabolism and hERG activity in this subseries could be resolved by fine-tuning physicochemical properties. Table 3 illustrates modifications made in the benzolactam subseries.

Examination of the X-ray crystal structure of **12** bound to XIAP (Figure 3A) suggested that addition of a substituent in the benzene ring of the isoindolinone ring system would be tolerated at C4, C5, and C6. A fluorine scan was carried out,

resulting in compounds **15**–**17** with improved XIAP affinity and satisfactory profiles in the CYP3A4 and hERG assays (Table 3). Of these, **17** had the most balanced XIAP/cIAP1 profile, comparable to **5**, and was progressed to in vivo PK evaluation. Oral bioavailability in mouse was 3%, comparable with **14**, so the compound was not progressed further. Substitution with the more polar cyano group at C5 and C6, **18** and **19** respectively, gave satisfactory CYP3A4 and hERG profiles and was reasonably well tolerated with respect to XIAP affinity. However, these changes resulted in lower activity in both cIAP1 degradation assay and MDA-MB-231 antiproliferation assays compared with the corresponding fluoro derivatives.

Table 4 illustrates changes made in the P2 morpholine subseries. The optimization strategy adopted here involved performing a polar substituent scan in positions that were (i) capable of disrupting the hERG pharmacophore and (ii) considered to be most accommodating with respect to the X-ray crystal structure of **5** bound to XIAP. With a view to minimizing added molecular weight, priority was given to addition of a hydroxy substituent and introduction of a carbonyl group in the pyridyl ring to form a pyridone. Dimethylmorpholine **8**, having the highest XIAP and cIAP1 potency, was chosen as the baseline compound for this work, and data are shown in Table 4. The main areas of opportunity were on the periphery of the P4 pocket and the aromatic portion of the azaindole bicycle. A diastereomeric pair of  $\alpha$ -hydroxylated P4 4-fluorobenzyl derivatives was prepared **20** and **21**, with the latter having the higher affinity in the XIAP cell-based IP assay. The additional hydroxyl group also had a beneficial effect on CYP3A4 stability, and this translated into improved bioavailability in mouse (31% at 10 mg/kg) and, importantly, in cynomolgus monkey (13% at 5 mg/kg). Compound **21** also emphatically reduced hERG activity, with minimal inhibition in the PPC assay. However, the antiproliferative effect in MDA-MB-231 cells was weaker than **5**, reflecting a loss of potency in the cIAP1 degradation assay. Figure 3B shows the X-ray crystal structure of **21** bound to XIAP, from which the ligand electron density was consistent with the assigned absolute stereochemistry of the ligand at the benzylic carbon. The ligand adopts a binding mode similar to that of **5**, with the benzyl moiety occupying the P4 pocket and the hydroxyl group well accommodated. However, when the cIAP1 protein structure is overlaid with the **21**–XIAP complex (Figure 3C), a clash is apparent with the side chain of cIAP1 Arg308. This arginine residue is presumed to be quite rigid, being involved in a salt bridge with the carboxy side chain of Asp297. Binding of **21** to cIAP1 may therefore require disruption of the salt bridge and thus incur an energetic penalty. In XIAP by contrast, the residue corresponding to Arg308 is much smaller, namely, Thr308. Hence the differential effects on XIAP and cIAP1 activity can be rationalized in terms of a residue difference in close proximity to the P4 pocket. Incorporation of hydroxyl in the aromatic portion of the P4 substituent **22** is well-tolerated with respect to cIAP1 but not XIAP, resulting in an unbalanced profile. Hence addition of polarity to the P4 substituent did not optimally achieve the target profile, and we turned our attention to the azaindoline scaffold.

Efforts were focused primarily on the 4-azaindoline core, with C5 offering the opportunity to add polar substitution. Formal hydroxylation of the azaindoline scaffold at C5 to give the pyridone **23** was well tolerated with respect to XIAP

affinity in the cellular IP assay ( $IC_{50}$  5.4 nM). However, this change also resulted in exceptionally high cIAP1 potency in the degradation assay ( $IC_{50}$  130 pM) and, consequently, an unbalanced XIAP/cIAP1 profile. There was, encouragingly, an improvement in metabolic stability in the CYP3A4 turnover assay and reduced hERG inhibition. *N*-Methylation of the pyridone **24** surprisingly gave a much more balanced profile, largely due to a significant increase in XIAP affinity, without increasing hERG inhibition, though stability in the CYP3A4 assay was suboptimal. These observations for CYP3A4 are consistent with an increase in lipophilicity for **24**, the ChlogD value of 3.2 being slightly above the limit suggested by the model described above. The absence of a similar deleterious effect on hERG may be due to effective disruption of the hERG pharmacophore by the presence of the pyridone carbonyl group. The isomeric pyridone **25** was also investigated, where the pyridone nitrogen constitutes the growth point for the P4 side chain, but this change proved ineffective for XIAP potency.

Having seen some encouraging effects on metabolic turnover and hERG inhibition from addition of an oxygen substituent, we examined incorporation of hydroxymethyl substitution at azaindoline C5. The prototype compound **26** resulted in a modest increase in potency compared to **8**. However, CYP3A4 stability and hERG inhibition were not optimized, ascribed to the relatively high lipophilicity of the molecule (ChlogD 3.5), beyond the upper limit of our targeted range. The exceptional potency of **26** allowed some headroom for sacrifice of primary activity in the pursuit of better physicochemical properties. Removal of a methyl group from the morpholine gave **27**,<sup>19</sup> with XIAP cellular  $IC_{50}$  2.8 nM (LE 0.30), cIAP1 degradation  $IC_{50}$  0.22 nM, and potent antiproliferative effect in the MDA-MB-231 assay ( $IC_{50}$  1.8 nM). The ratio of cIAP1 to XIAP potency for **27** (13-fold) was similar to the lead **5** and therefore met our target for a relatively balanced IAP antagonist profile. Compound **27** has also been shown to cause degradation of both cIAP1 and cIAP2 in the diffuse large B-cell lymphoma cell line, WSU-DLCL2, which has a high basal level of cIAP2.<sup>19</sup> In the hERG PPC assay, **27** gave 30% inhibition at 30  $\mu$ M and  $IC_{50}$  69  $\mu$ M. Compound **27** was subsequently profiled in a cardiovascular study in conscious cynomolgus monkeys and showed no effect on QT interval (corrected for heart rate) at all doses up to a maximum tolerated single oral dose of 100 mg/kg. In the CYP3A4 turnover assay, **27** had improved metabolic stability compared to **5**, despite retaining the morpholine P2 substituent. Therefore, it was gratifying that, in addition to having acceptable oral bioavailability in mouse (34% at 10 mg/kg), **27** had significantly improved oral exposure in cynomolgus monkey compared to **5** (F 12% at 5 mg/kg rising to 50% at 60 mg/kg). Table 5 shows the cross-species pharmacokinetic data for **27**. Compound **27** was subsequently selected as a clinical drug candidate, having a balanced IAP antagonist profile, improved oral bioavailability in NHP with respect to **5** and acceptable preclinical cardiac safety profile. Antagonism of cIAP1 and XIAP by **27** along with antitumor activity in cell lines and xenograft models has been recently described.<sup>19</sup> For example, significant cIAP1 and XIAP antagonism was observed for up to 72 h in the MDA-MB-231 xenograft model following a single 20 mg/kg oral dose of **27** (Figure 5A). These pharmacodynamic effects correlated with compound levels detected in the tumor throughout the duration of the experiment. Inhibition of tumor growth was

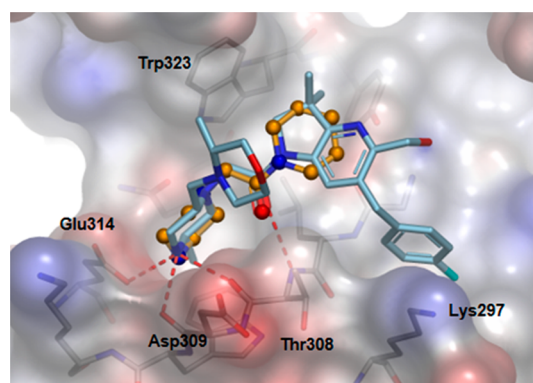
**Table 5. Cross-Species Pharmacokinetic Parameters for Compound 27**

species <sup>a</sup>	CL <sub>p</sub> mL min <sup>-1</sup> kg <sup>-1</sup>	V <sub>ss</sub> L kg <sup>-1</sup>	C <sub>max</sub> (PO) ng mL <sup>-1</sup>	F%
mouse	41	2.7	433	34
rat	38	9.3	117	29
cynomolgus monkey	16	6.0	137	12

<sup>a</sup>Plasma clearance (CL<sub>p</sub>), volume of distribution at steady state (V<sub>ss</sub>), maximum concentration in plasma (C<sub>max</sub>), and oral bioavailability (F) were determined using an intravenous (IV) dose of either 1 mg/kg (cynomolgus monkey) or 5 mg/kg (mouse, rat) and an oral (PO) dose of either 5 mg/kg (cynomolgus monkey) or 10 mg/kg (mouse, rat). For assay details, see [Experimental Section](#).

also demonstrated in the MDA-MB-231 model following oral daily dosing of 27 as the hydrochloride and L-lactate salt ([Figure 5B](#)).

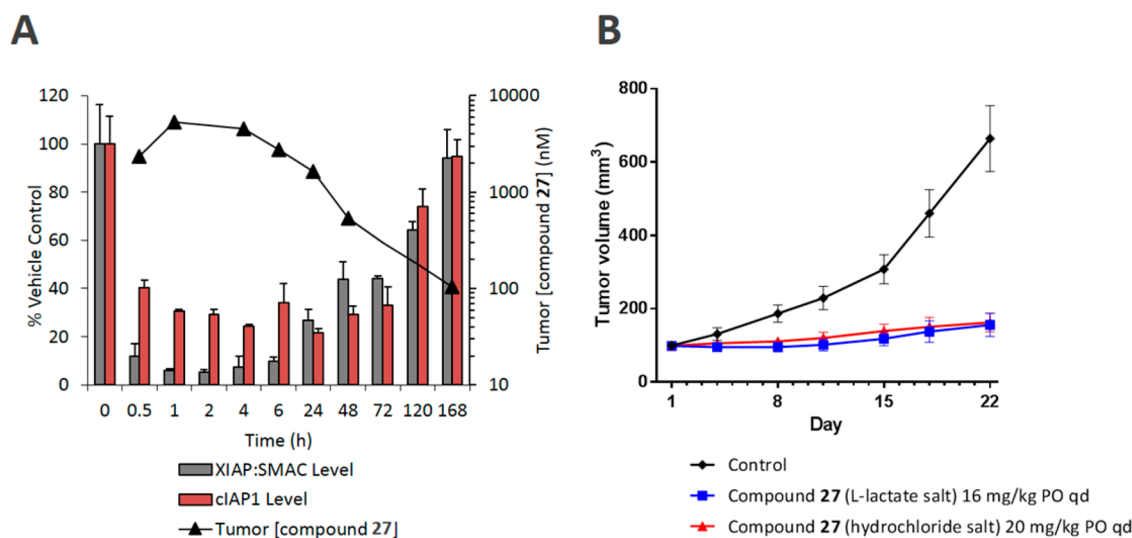
The binding mode of 27 in XIAP (PDB code 5OQW) has been described,<sup>19</sup> and it is instructive to compare the interactions made by the clinical candidate with those of the original fragment hit 6<sup>17</sup> ([Figure 6](#)). Notably all polar interactions made by the fragment are conserved in the binding mode of 27 and all additional protein–ligand contacts are hydrophobic in nature. In particular the P2 2-methylmorpholine only makes contact with the protein via the methyl group. Protein–protein interaction surfaces tend to be highly lipophilic and it can be challenging to design antagonists with favorable physicochemical properties. The morpholine moiety here makes an important contribution to controlling lipophilicity, although the primary importance of this group lies in (i) its ability to stabilize the active ligand conformation and (ii) shield the key polar interaction of the amide carbonyl with the backbone NH of Thr308, as has previously been discussed.<sup>18</sup> A surprising aspect of the optimization from 5 to 27 is that success was achieved in terms of metabolic stability despite leaving the metabolically



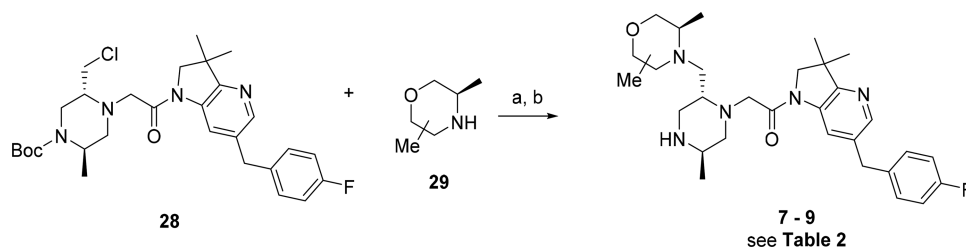
**Figure 6.** X-ray crystal structure of 27 (cyan) bound to XIAP (PDB 5OQW) overlaid in same frame of reference as the XIAP complex with fragment hit 6. Compound 6 is displayed as orange balls and sticks. Hydrogen bonds are shown as dashed red lines and the displayed protein Connolly surface is colored by electrostatic potential (blue = positive, red = negative).

most labile group intact; attempts to add blocking groups or replace with alternative P2 substituents were less successful with respect to overall profile. The key enabler in the morpholine subseries with respect to CYP3A4 stability and hERG inhibition was research utilizing crystal structure information to help identify positions where polar substitution would be most optimally tolerated. The positioning of a hydroxymethyl group on the 4-azaindoline core, proximal to the hydrophobe feature in the Aaronov pharmacophore (green sphere in [Figure 2B](#)), offered the best balance between desired XIAP and cIAP1 target profiles, as well as providing optimized metabolic and cardiac profiles.

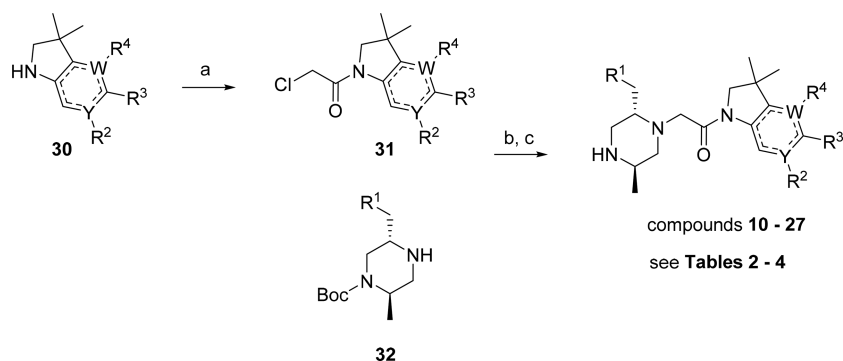
Several synthetic challenges needed to be addressed in order to access the growing vectors for optimal pocket filling. First, for the P1 and P2 region, a stereospecific synthesis of substituted piperazines was required. Second, for the P3 and P4 region, a reliable method for constructing a range of



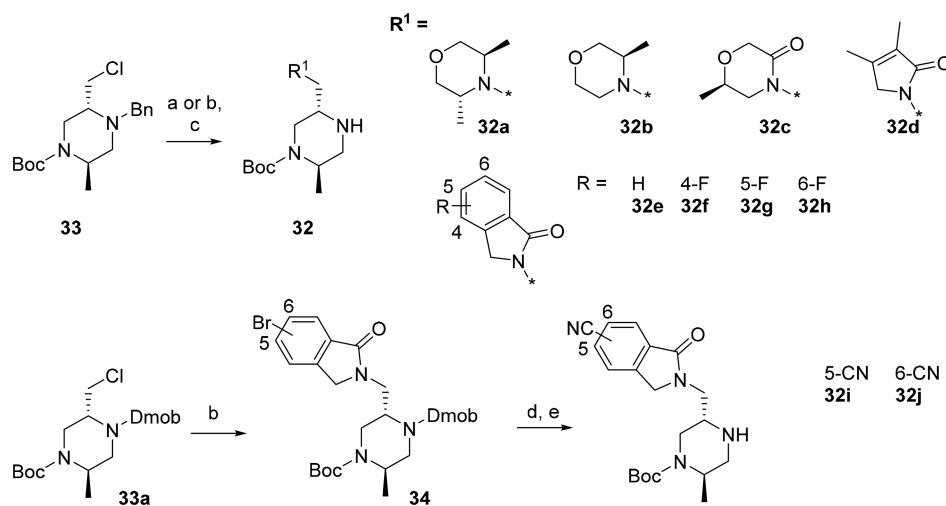
**Figure 5.** Pharmacodynamic and tumor growth inhibitory effects of 27 (ASTX660) in MDA-MB-231 xenograft mouse model. (A) Antagonism of XIAP (gray bars) and cIAP1 (red bars) over a seven-day time course following a single 20 mg/kg oral dose of 27 (free base equivalent, hydrochloride). Quantification of XIAP:SMAC complex and cIAP1 levels in the tumor lysate was performed using a Mesoscale Discovery (MSD) platform. The black triangles denote concentration of 27 in tumor during the time course of the same experiment. (B) Tumor growth inhibitory activity of 27 in MDA-MB-231 xenograft model following daily (qd) oral (PO) dosing with 27 at 16 mg/kg (free base equivalent, L-lactate salt) and 20 mg/kg (free base equivalent, hydrochloride salt). Test article was dosed on days 1–21 inclusive.

Scheme 1<sup>a</sup>

<sup>a</sup>Reagents and conditions: (a)  $K_2CO_3$ , KI, MeCN, 90 °C, 31–64%; (b) HCl, dioxane, EtOAc, RT, 59–86%.

Scheme 2<sup>a</sup>

<sup>a</sup>Reagents and conditions: (a)  $ClCH_2COCl$ , MeCN, ~ 5 °C, used without purification; (b)  $K_2CO_3$ , KI, MeCN, 0 °C - RT, 55–98%; (c) HCl, dioxane, EtOAc, RT, 58–100%.

Scheme 3<sup>a</sup>

<sup>a</sup>Reagents and conditions: (a)  $R^1H$ ,  $K_2CO_3$ , KI, MeCN, 70 °C, 94% (for 32a, 32b); (b)  $R^1H/NaH$ , DMF, RT then 80 °C, 20–69% (for 32c–32h, 34); (c)  $H_2$ , Pd/C, EtOH, HOAc, RT, 72–100%; (d)  $Zn(CN)_2$ ,  $Pd_2(dba)_3$ ,  $Pd(PPh_3)_4$ , dppf, DMF, water, 100 °C, 75%; (e) TFA, RT then  $(Boc)_2O$ ,  $Et_3N$ , MeOH, 0 °C - RT, 41%.

heterobicyclic scaffolds had to be developed, together with appropriate C–C bond formation and functionalization methods. Some of this work has been described previously.<sup>18,25</sup>

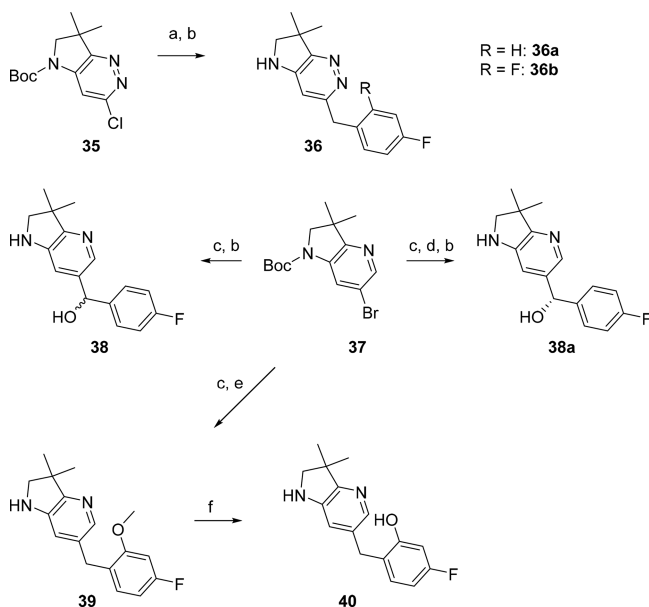
Compounds 7–27 in Tables 2–4 were synthesized as shown in Schemes 1–6 using a strategy similar to that described for 5.<sup>18</sup> Full experimental details are provided in Supporting Information. For 7–9, the substituted morpholine P2 substituent was introduced at a late stage in the synthesis by reaction of previously reported chloro derivative 28<sup>18</sup> with the appropriate amine 29 (Scheme 1). Subsequent acid-mediated Boc deprotection gave desired targets 7–9 as hydrochloride

salts. Preparation of all other compounds followed the more convergent route shown in Scheme 2 involving a two stage, three-component coupling, whereby a heterobicyclic precursor 30 was chloroacetylated and the resulting chloroamide 31 aminated with a protected piperazine 32 in which the desired P2 substituent had already been installed. Removal of the Boc protection as described above afforded the desired targets 10–27 as hydrochloride salts.

Substituted piperazine coupling partners 32 were prepared according to Scheme 3, by reaction of orthogonally protected chloropiperazine 33<sup>18</sup> with the appropriate cyclic amine or

amide under basic conditions and subsequent hydrogenolysis of the benzyl moiety. For the cyano substituted isoindolinones **32i** and **32j**, the synthesis began with 2,4-dimethoxybenzyl (Dmob) protected piperazine **33a** (prepared in an analogous method to that for **33**) and involved reaction with the sodium salt of the appropriate bromoisoindolinone, followed by palladium mediated cyanation of adducts **34**, global deprotection, then reattachment of the Boc group to give **32i** and **32j**.

Heterobicyclic coupling precursors **30** were either prepared in the manner previously disclosed<sup>18</sup> (e.g., those for compounds **10–12**) or using the methods shown in Schemes 4–6. For fused pyridazine containing compounds such as **13**,

Scheme 4<sup>a</sup>

<sup>a</sup>Reagents and conditions: (a) ArZnCl, LiBr, PEPPSI-IPr, NMP, THF, 20 °C, used without purification; (b) HCl<sub>aq</sub>, MeOH, 20–50 °C, 90–100% over 2 steps; (c) BuLi, hexanes, THF, –78 °C, 0.5 h then appropriate substituted benzaldehyde, –78 °C, 0.5 h, 82–93%; (d) chiral HPLC separation; (e) TMSCl, NaI, MeCN, 60 °C, 6 h, 44%; (f) BBr<sub>3</sub>, CH<sub>2</sub>Cl<sub>2</sub>, RT, 66%.

Boc protected chloro precursor **35**<sup>25</sup> (Scheme 4) was subjected to Negishi coupling with the appropriately substituted benzylzinc chloride, and the resulting product was treated with acid to give the desired coupling partners **36** in high yield. For compounds bearing a hydroxy group in the P4 substituent, bromo-bicycle **37** proved to be a useful starting point (Scheme 4). Lithium halogen exchange followed by quench with 4-fluorobenzaldehyde gave an enantiomeric mixture of secondary alcohols. Boc deprotection gave the racemic alcohol precursor **38**, which was used in the initial small-scale preparation of **20** and **21**, where the epimeric mixture of final compounds was separated by chiral HPLC. Alternatively, for preparation of larger quantities of **21**, chiral separation was performed on the Boc protected 4-fluorobenzaldehyde adduct, and this was followed by Boc deprotection of the desired (*S*)-enantiomer to afford precursor **38a**. Similarly, the anion derived from **37** could be quenched with 2-methoxy-4-fluorobenzaldehyde, and the resulting racemic mixture of alcohols was treated with chlorotrimethylsilane and sodium iodide<sup>26</sup> to give methoxy derivative **39**. Demethylation was then effected using boron

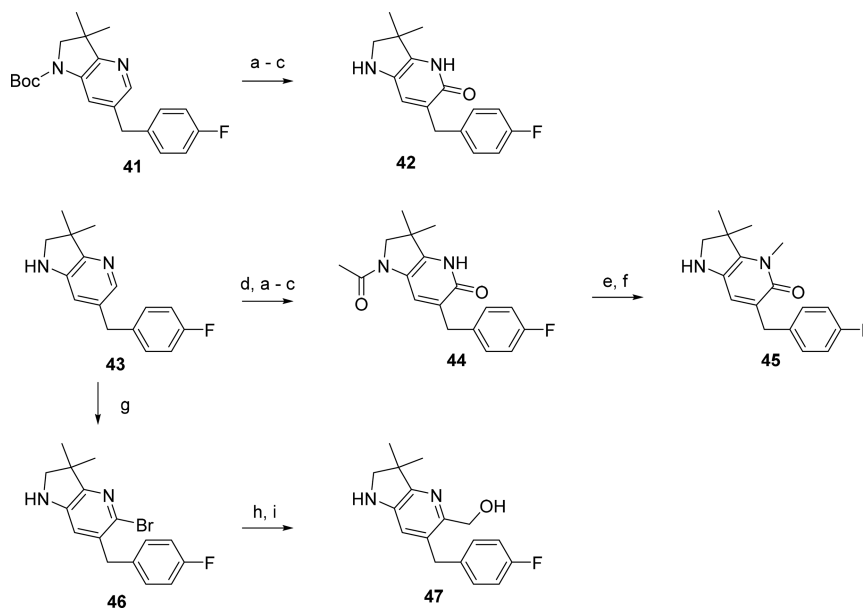
tribromide in dichloromethane to give hydroxy substituted coupling partner **40**.

Previously reported azaindolines **41** and **43**<sup>18</sup> proved to be useful starting points for the preparation of the corresponding pyridone precursors **42** and **45** (Scheme 5). Treatment of **41** with 3-chloroperbenzoic acid resulted in N-oxidation, and this product was rearranged to the pyridone using acetic anhydride followed by base hydrolysis. Acid treatment then removed the Boc group to give desired coupling precursor **42**. For the *N*-methylated pyridone **45**, the more stable acetyl protecting group was required. Acetylation of **43** proceeded in high yield, and an oxidation–rearrangement sequence as described above gave pyridone **44**. Methylation was performed using iodomethane in the presence of base, albeit in modest yield, and the acetyl protecting group was removed using acid treatment at elevated temperature. Building block **43** also allowed access to hydroxymethyl derivative **47** (Scheme 5), by virtue of the relatively high reactivity of the azaindoline C5 position toward electrophiles. Thus, treatment with *N*-bromosuccinimide gave bromo compound **46** in high yield, and then two-stage lithiation using methyllithium (which removed the proton from N1) followed by *tert*-butyllithium and subsequent quench at low temperature with *N,N*-dimethylformamide gave the C5 substituted aldehyde. This product, used without further purification, was reduced with sodium borohydride to give coupling partner **47**. This three-stage procedure proceeded in good overall yield and has proved highly suitable for large scale synthesis (>1 kg).

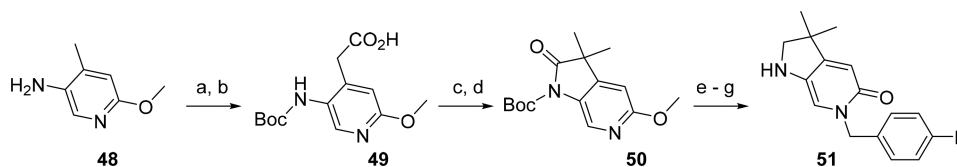
In order to access the isomeric pyridone coupling partner **51** required for **25**, a de novo ring synthesis was required (Scheme 6). Commercially available substituted pyridine **48** was Boc protected then treated with an excess of *sec*-butyllithium to form the C-lithio species. Quenching with carbon dioxide gas then gave acid **49**. Lactam formation under standard amide bond forming conditions was followed by treatment with iodomethane under basic conditions to give the 3,3-dimethyl derivative **50**. Quaternization of the pyridine nitrogen with 4-fluorobenzyl bromide followed by in situ demethylation introduced the pyridone functionality, and the remaining steps involved Boc deprotection and selective reduction of the lactam carbonyl to furnish desired intermediate **51**.

## CONCLUSIONS

Starting from a millimolar affinity fragment **6**, compound **27** has been identified having a balanced antagonist profile for cIAP1 and XIAP and suitable profile for progression into the clinic. Multiple structure-based techniques were used, such as X-ray crystallography, computational modeling, and NMR-guided conformational analysis. By employing a fragment-based as opposed to a peptidomimetic strategy, and focusing the FBDD optimization around the XIAP crystal structure, the intrinsic high cIAP1 selectivity resulting from approaches based on the AVPI tetrapeptide has been avoided. The value of experimental research and development focusing on crystal structures and biological data can be valuable in guiding affinity optimization in FBDD. However, as shown here, structural information can also be helpful in directing multiple changes which result in various compounds having desirable potency, while improving hERG and metabolism profiles. After extensive testing, the successful optimization ultimately involved making important but relatively small structural changes to **5**, including substituent scanning with polar groups which carried with them remarkable impact in terms of

Scheme 5<sup>a</sup>

<sup>a</sup>Reagents and conditions: (a) 3-chloroperbenzoic acid,  $\text{CH}_2\text{Cl}_2$ , RT, 65%; (b) 1.  $\text{Ac}_2\text{O}$ , 105–140 °C; 2.  $\text{NaOH}_{\text{aq}}$ , MeOH, RT, 100%; (c)  $\text{HCl}_{\text{aq}}$ , MeOH, reflux, 59%; (d)  $\text{Ac}_2\text{O}$ , MeCN, RT, 100%; (e) MeI,  $\text{K}_2\text{CO}_3$ , DMF, 0 °C – RT, 29%; (f)  $\text{HCl}_{\text{aq}}$ , EtOH, 95 °C, used without purification; (g) *N*-bromosuccinimide, DMF, 5 °C – RT, 95%; (h) 1. MeLi,  $\text{Et}_2\text{O}$ , THF, –78 °C; 2. *tert*-BuLi, hexane; 3. DMF, –78 °C, used without purification; (i)  $\text{NaBH}_4$ , MeOH, ~ 5 °C, 76% over 2 steps.

Scheme 6<sup>a</sup>

<sup>a</sup>Reagents and conditions: (a)  $(\text{Boc})_2\text{O}$ ,  $\text{Na}_2\text{CO}_3$ ,  $\text{H}_2\text{O}$ , THF, RT, 100%; (b) *sec*-butyllithium, cyclohexane, THF, –78 °C then  $\text{CO}_2(\text{g})$ , 100%; (c) EDC, HOAT,  $i\text{Pr}_2\text{NEt}$ ,  $\text{CH}_2\text{Cl}_2$ , RT, 70%; (d) MeI,  $\text{K}_2\text{CO}_3$ , acetone, reflux, 68%; (e) 4-fluorobenzyl bromide, NaI, MeCN, reflux, 11 h, 48%; (f) TFA,  $\text{CH}_2\text{Cl}_2$ , RT, 90%; (g)  $\text{BH}_3\cdot\text{Me}_2\text{S}$ , THF, Reflux, 99%.

optimizing hERG and metabolism. For example, the structural difference between **5** and **27** is quite small, namely, the addition of a single two heavy atom substituent, but this change had a profoundly beneficial effect on the metabolic and hERG parameters, as well as resulting in a small but significant improvement in IAP antagonist activity. Throughout the rigorous testing, the combination of structural knowledge and control of physicochemical properties proved critical to the identification of the clinical candidate. Compound **27** (ASTX660) is now being evaluated in a phase 1/2 study in subjects with advanced solid tumors and lymphomas (NCT02503423). Additional clinical studies with **27** will further explore the therapeutic potential of this novel IAP antagonist, both as a single agent and in combination.

## EXPERIMENTAL SECTION

**General Chemistry.** All solvents employed were commercially available anhydrous grade, and reagents were used as received unless otherwise noted. Hereafter, petrol denotes the petroleum ether fraction boiling at 40–60 °C. Flash column chromatography was performed on a Biotage SP1 system (32–63  $\mu\text{m}$  particle size, KP-Sil, 60 Å pore size). NMR spectra were recorded on a Bruker AV400 (Avance 400 MHz) spectrometer. Analytical LC–MS was conducted using an Agilent 1200 series with Mass Spec Detector coupled with an Agilent 6140 single quadrupole mass detector and an Agilent 1200

MWD SLUV detector. LC retention times, molecular ion ( $m/z$ ) and LC purity (by UV) were based on the method below. Purity of compounds (as measured by peak area ratio) was >95%, as determined by the LC method described below. High resolution mass spectrometry was performed on an Agilent 6550 Quadrupole Time-of-Flight mass spectrometer.

LC Method (BASIC)

Eluent A: 95:5 10 mM  $\text{NH}_4\text{HCO}_3$  +  $\text{NH}_4\text{OH}/\text{CH}_3\text{CN}$  (pH = 9.2)

Eluent B:  $\text{CH}_3\text{CN}$

Gradient: 5–95% eluent B over 1.1 min

Flow: 0.9 mL/min

Column: Waters Acquity UPLC BEH C18; 1.7  $\mu\text{m}$ ; 2.1 × 50 mm

Column T: 50 °C

**Preparation of Compound 27 (Schemes 2 and 5).** 1-(6-[(4-Fluorophenyl)methyl]-5-(hydroxymethyl)-3,3-dimethyl-1*H*,2*H*,3*H*-pyrrolo[3,2-*b*]pyridin-1-yl)-2-[(2*R*,5*R*)-5-methyl-2-[(3*R*)-3-methylmorpholin-4-yl)methyl]piperazin-1-yl]ethan-1-one dihydrochloride.

**Step 1:** 5-Bromo-6-(4-fluorobenzyl)-3,3-dimethyl-2,3-dihydro-1*H*-pyrrolo[3,2-*b*]pyridine **46**. A solution of 6-(4-fluorobenzyl)-3,3-dimethyl-2,3-dihydro-1*H*-pyrrolo[3,2-*b*]pyridine **43**<sup>18</sup> (88.5 g, 0.345 mol) in DMF (1.67 L) was cooled to –5 °C. Solid *N*-bromosuccinimide (61.5 g, 0.345 mol) was added in portions with exotherm. The mixture was stirred for 1 h warming to room temperature. Water (2.66 L) was added with exotherm and the resulting mixture was stirred for 18 h at room temperature. The solids were filtered and cake washed with water (270 mL). The filter cake was dissolved in THF (1.5 L), dried over  $\text{MgSO}_4$ , filtered and

concentrated *in vacuo* to give the title compound (109.7 g, 95%) as a yellow solid.  $^1\text{H}$  NMR (DMSO- $d_6$ ): 7.29–7.20 (2H, m), 7.20–7.03 (2H, m), 6.64 (1H, s), 5.88 (1H, s), 3.89 (2H, s), 3.26 (2H, d), 1.20 (6H, s). LCMS:  $[\text{M} + \text{H}]^+ = 335, 337$ .

**Step 2:** [6-(4-Fluoro-benzyl)-3,3-dimethyl-2,3-dihydro-1H-pyrrolo[3,2-b]pyridin-5-yl]-methanol **47**. To 5-bromo-6-(4-fluoro-benzyl)-3,3-dimethyl-2,3-dihydro-1H-pyrrolo[3,2-b]pyridine **46** (22.8 g, 68.2 mmol) in THF (300 mL), cooled to  $-78^\circ\text{C}$ , was added methylolithium (1.6 M in Et<sub>2</sub>O; 51.1 mL, 91.8 mmol) over 15 min *tert*-butyllithium (1.7 M in hexane; 96 mL, 164 mmol) was then added over 30 min. After 15 min, DMF (26 mL) was added, and the mixture was stirred at  $-78^\circ\text{C}$  for a further 50 min. Saturated aqueous NH<sub>4</sub>Cl (450 mL) was added, and the mixture was stirred for 10 min at RT. The organic layer was isolated, and the aqueous layer was extracted with EtOAc (2  $\times$  150 mL). The combined organic fractions were washed with brine (200 mL), dried (MgSO<sub>4</sub>) and evaporated to give 6-(4-fluoro-benzyl)-3,3-dimethyl-2,3-dihydro-1H-pyrrolo[3,2-b]pyridine-5-carbaldehyde as a yellow solid which was used without any further purification. LCMS:  $[\text{M} + \text{H}]^+ = 285$ . This product (~68 mmol) was suspended in MeOH (250 mL) and cooled in an ice bath. NaBH<sub>4</sub> (3.4 g, 81.8 mmol) was added portionwise over 5 min. Cooling was removed and the mixture was stirred for a further 20 min. The mixture was cooled in an ice bath followed by careful addition of 10% aqueous KHSO<sub>4</sub> over 10 min (care: effervescence). After stirring for 5 min at RT, the mixture was recooled using an ice bath. The mixture was basified by addition of 50% aqueous NaOH (~18 mL) and then concentrated *in vacuo* to approximately one-third volume. The resulting aqueous mixture was extracted with CH<sub>2</sub>Cl<sub>2</sub> (1  $\times$  200 mL, 2  $\times$  100 mL), and the combined CH<sub>2</sub>Cl<sub>2</sub> layers were dried (MgSO<sub>4</sub>). The CH<sub>2</sub>Cl<sub>2</sub> solution was concentrated *in vacuo* to ~30 mL and then diluted with toluene (70 mL) to initiate crystallization of the product. Collection by filtration gave the product as a colorless crystalline solid (10.6 g). A second crop (2.1 g) was collected from the filtrate. The filtrate was concentrated, and the remaining material was purified by SiO<sub>2</sub> chromatography (eluting with 25–50% EtOAc/hexanes) to give a third batch of material (2.1 g), giving the title compound in an overall yield of 14.8 g (76% over 2 steps).  $^1\text{H}$  NMR (400 MHz, CDCl<sub>3</sub>): 7.13–7.05 (2H, m), 7.05–6.89 (2H, m), 6.60 (1H, s), 4.79 (1H, t), 4.61 (2H, d), 3.78 (2H, s), 3.65 (1H, s), 3.41 (2H, d), 1.36 (6H, s). LCMS:  $[\text{M} + \text{H}]^+ = 287$ .

**Step 3:** 2-Chloro-1-(6-[(4-fluorophenyl)methyl]-5-(hydroxymethyl)-3,3-dimethyl-1H,2H,3H-pyrrolo[3,2-b]pyridin-1-yl)ethan-1-one. To a cooled (~5  $^\circ\text{C}$ ) suspension of [6-(4-fluoro-benzyl)-3,3-dimethyl-2,3-dihydro-1H-pyrrolo[3,2-b]pyridin-5-yl]-methanol **47** (11.8 g, 41.3 mmol) in MeCN (175 mL) was added chloroacetyl chloride (6.9 mL, 86.7 mmol). Cooling was removed and the mixture was stirred for 30 min at RT. The mixture was then evaporated *in vacuo* and dissolved in MeOH (200 mL). K<sub>2</sub>CO<sub>3</sub> solution (12 g in 100 mL H<sub>2</sub>O) was added, and the mixture was stirred at RT for 20 min after which the mixture was concentrated *in vacuo* to approximately one-quarter volume. The aqueous mixture was extracted with CH<sub>2</sub>Cl<sub>2</sub> (1  $\times$  100 mL, 2  $\times$  30 mL), and the combined CH<sub>2</sub>Cl<sub>2</sub> layers were dried (MgSO<sub>4</sub>). Evaporation *in vacuo* gave the title compound as colorless crystalline solid (12.1 g, 99%).  $^1\text{H}$  NMR (400 MHz, Me- $d_3$ -OD): 8.18 (1H, s), 7.21 (2H, dd), 7.08–6.98 (2H, m), 4.70 (2H, s), 4.39 (2H, s), 4.11 (2H, s), 4.03 (2H, s), 1.43 (6H, s). LCMS:  $[\text{M} + \text{H}]^+ = 363$ .

**Step 4:** *tert*-Butyl (2R,5S)-4-(2-(6-[(4-fluorophenyl)methyl]-5-(hydroxymethyl)-3,3-dimethyl-1H,2H,3H-pyrrolo[3,2-b]pyridin-1-yl)-2-oxoethyl)-2-methyl-5-((3R)-3-methylmorpholin-4-yl)methyl)piperazine-1-carboxylate. (2R,5S)-2-Methyl-5-((R)-3-methylmorpholin-4-yl)methyl)piperazine-1-carboxylic acid *tert*-butyl ester **32b**<sup>18</sup> (15.5 g, 46.4 mmol), KI (12.8 g, 77.4 mmol), and K<sub>2</sub>CO<sub>3</sub> (21.4 g, 155 mmol) were stirred in MeCN (70 mL) and cooled in an ice bath. 2-Chloro-1-(6-[(4-fluorophenyl)methyl]-5-(hydroxymethyl)-3,3-dimethyl-1H,2H,3H-pyrrolo[3,2-b]pyridin-1-yl)ethan-1-one (14.0 g, 38.7 mmol) was then added as a solution in MeCN (100 mL). The mixture was stirred at RT for 2 h and then concentrated *in vacuo* to approximately one-quarter volume. The mixture was partitioned between EtOAc (150 mL) and H<sub>2</sub>O (150 mL), and then the aqueous

layer was extracted with further EtOAc (1  $\times$  75 mL). The combined EtOAc layers were washed with 10% aqueous KH<sub>2</sub>PO<sub>4</sub> (4  $\times$  100 mL) and then brine (70 mL). The organic layer was dried (MgSO<sub>4</sub>) and evaporated to give the product as a colorless solid (25.8 g, 98%).  $^1\text{H}$  NMR (400 MHz, Me- $d_3$ -OD): 8.17 (1H, s), 7.21 (2H, dd), 7.03 (2H, t), 4.71 (2H, s), 4.23–4.15 (1H, m), 4.11–3.96 (4H, m), 3.80–3.51 (5H, m), 3.30–3.21 (2H, m), 3.01–2.63 (4H, m), 2.61–2.43 (2H, m), 2.37 (1H, t), 2.31–2.17 (1H, m), 1.47 (9H, s), 1.43 (6H, s), 1.25–1.22 (3H, m), 1.01 (3H, d). LCMS:  $[\text{M} + \text{H}]^+ = 640$ .

**Step 5:** 1-(6-[(4-Fluorophenyl)methyl]-5-(hydroxymethyl)-3,3-dimethyl-1H,2H,3H-pyrrolo[3,2-b]pyridin-1-yl)-2-[(2R,5R)-5-methyl-2-((3R)-3-methylmorpholin-4-yl)methyl)piperazin-1-yl]ethan-1-one dihydrochloride **27**. A mixture of *tert*-butyl (2R,5S)-4-(2-(6-[(4-fluorophenyl)methyl]-5-(hydroxymethyl)-3,3-dimethyl-1H,2H,3H-pyrrolo[3,2-b]pyridin-1-yl)-2-oxoethyl)-2-methyl-5-((3R)-3-methylmorpholin-4-yl)methyl)piperazine-1-carboxylate (0.47 g), ethyl acetate (10 mL) and HCl–dioxane (4 M; 10 mL) was stirred at 20  $^\circ\text{C}$  for 18 h, and the resulting solid was collected by filtration to give the title compound (0.43 g, 95%) as a colorless solid.  $[\alpha]_{\text{D}}^{20}$  10 $^\circ$  (c 1.00, EtOH),  $^1\text{H}$  NMR (400 MHz, Me- $d_3$ -OD): 8.56 (1H, s), 7.34 (2H, dd), 7.15 (2H, dd), 5.00 (2H, s), 4.33–4.19 (4H, m), 4.18–3.92 (5H, m), 3.83–3.38 (8H, m), 3.16 (4H, m), 1.65 (6H, s), 1.46 (3H, d), 1.38–1.25 (3H, m).  $^{13}\text{C}$  NMR (101 MHz, DMSO- $d_6$ )  $\delta$  170.43, 160.73 (d,  $J = 241.7$  Hz), 156.09, 152.12, 136.43 (d,  $J = 3.1$  Hz), 135.06, 133.41, 130.59 (d,  $J = 8.0$  Hz), 123.91, 115.09 (d,  $J = 21.1$  Hz), 72.06, 66.25, 63.26, 59.92, 58.26, 56.12, 55.62 (broad), 55.34, 51.70, 51.60, 50.52, 48.97, 40.47, 35.37, 27.22, 26.90, 17.54, 13.43 (broad) [ $^{13}\text{C}$  NMR data acquired on free base due to broad signals seen for dihydrochloride]. HRMS (ESI-QTOF):  $m/z$   $[\text{M} + \text{H}]^+$  Calcd for C<sub>30</sub>H<sub>42</sub>FN<sub>5</sub>O<sub>3</sub> 540.3344; Found 540.3345.  $\Delta = 0.19$  ppm. LCMS:  $[\text{M} + \text{H}]^+ = 540$ .

**Derivation of Chromatographic LogD (ChlogD  $\equiv$  ChromLogD<sub>7.4</sub>).** Chromatographic hydrophobicity index (CHI) values were measured using reversed phase HPLC column (PolymerX RP-1, Phenomenex, UK) with a fast acetonitrile gradient at starting mobile phase of pH = 7.4. CHI values are derived directly from the gradient retention times by using a calibration line obtained for standard compounds. The CHI value approximates to the volume % organic concentration when the compound elutes. CHI is linearly transformed into ChromLogD<sub>7.4</sub> (abbreviated to ChlogD in main text of article) by least-squares fitting of experimental CHI values to calculated C logP values for over 20 000 research compounds using the following formula: ChromLogD<sub>7.4</sub> = 0.0857CHI-2.00. The average error of the assay is  $\pm 3$  CHI unit or  $\pm 0.25$  ChromLogD<sub>7.4</sub>.

**Crystallography.** XIAP-BIR3 250–354 was crystallized using a 1:1 ratio of 10 mg/mL protein and 0.1 M Hepes-NaOH pH 8.0, 3.0–3.9 M NaCl. Crystals appeared over the course of a few days at 4  $^\circ\text{C}$ . Crystals were soaked in fragments using 2.5  $\mu\text{L}$  of compound in 100% DMSO, 47.5  $\mu\text{L}$  of 0.1 M Hepes-NaOH pH 8.0, 4 M NaCl to give a final concentration of fragment in the range of 50–100 mM. The pH of the soaking solution was adjusted if necessary, and crystals were left at 4  $^\circ\text{C}$  for 24–72 h. Crystals were cryoprotected using 0.05 M Hepes-NaOH pH 8.0, 4 M NaCl, 15% ethylene glycol. The crystals had cell dimensions of approximately 70  $\text{\AA}$ , 70  $\text{\AA}$ , 105  $\text{\AA}$ , and belong to space group P4122. The diffraction observed ranged from 1.7 to 3.0  $\text{\AA}$ .

**Cell Line Proliferation Assay.** Inhibition of cell growth was measured using the Alamar Blue assay.<sup>27</sup> For each proliferation assay cells were plated onto 96 well plates and allowed to recover for 16 h prior to the addition of inhibitor compounds (in 0.1% DMSO v/v) for a further 72 h. At the end of the incubation period 10% (v/v) Alamar Blue (Bio-Rad AbD Serotec, Oxford, UK) was added and incubated for a further 6 h prior to determination of fluorescent product at 535 nM excitation/590 nM emission.

The antiproliferative activity of test compounds was determined by measuring the ability of the compounds to inhibit growth in two cancer cell lines: (1) MDA-MB-231 (human breast carcinoma) [ECACC, Salisbury, UK], (2) HCT116 (human colon carcinoma) [ECACC, Salisbury, UK] - insensitive cell line used as a control for nonspecific cytotoxicity.

The MDA-MB-231 proliferation data reported in the paper are the result of two duplicates. Compounds **2**, **5**, and **27** were tested multiple times in independent experiments and statistical limits are calculated for those compounds:

**2**:  $IC_{50} = 7.8$  nM, SD = 3.4,  $n = 6$ .

**5**:  $IC_{50} = 4.4$  nM, SD = 1.9,  $n = 21$ .

**27**:  $IC_{50} = 1.8$  nM, SD = 1.0,  $n = 4$ .

For HCT116 negative control cell proliferation data on compounds **5** and **7–27**; see Supporting Information Table S1.

**XIAP Antagonism Immunoprecipitation Assay.** An engineered HEK293 cell line was generated by transfecting the HEK293 cell line (ECACC, Salisbury, UK) with a full-length FLAG-tagged XIAP expression construct [Origene Technologies Inc., Rockville, USA] and a full-length untagged caspase-9 construct [Origene Technologies, Inc., Rockville, USA]. Stable cotransfectants were selected after culture in selection medium containing Geneticin (Life Technologies, Paisley, UK).

Stable HEK293-XIAP-Caspase-9 cells were plated out into 96-well plates and left overnight at 37 °C to recover. Compounds were added to duplicate wells in 0.1% DMSO for 2 h at 37 °C. Cells were lysed in 50  $\mu$ L lysis buffer (1% Triton X-100 in 20 mM Tris.Cl (pH 7.6), 150 mM NaCl, including protease inhibitors (Roche Diagnostics Ltd., Burgess Hill, UK) for 20 min rocking at room temperature. Streptavidin-coated high-bind MSD plates (Meso Scale Discovery, Gaithersburg, USA) were coated with biotinylated anti-FLAG M2 antibody (Sigma, Poole, UK) and then blocked with 3% BSA in TBST (20 mM Tris.Cl (pH 7.6), 150 mM NaCl, 0.1% Tween-20). Cell lysate was added to the 96-well anti-FLAG coated MSD plate and placed on a shaker overnight at 4 °C. After washing 3 times with TBST, rabbit anti-Caspase-9 (Cell Signaling Technology Inc., Danvers, USA) was added for 2 h at room temperature, with shaking. After washing three times with TBST, antirabbit-sulfo tag (Meso Scale Discovery, Gaithersburg, USA) was added for 2 h at RT. Plates were washed three times with TBST and then read buffer was added, before reading the plate on a MESO QuickPlex SQ 120 (Meso Scale Discovery, Gaithersburg, USA). The data reported in the paper are the result of two duplicates. Compounds **2**, **5**, and **27** were tested multiple times in independent experiments, and statistical limits were calculated for those compounds:

**2**: XIAP IP  $EC_{50} = 35$  nM, SD = 12,  $n = 6$ .

**5**: XIAP IP  $EC_{50} = 5.1$  nM, SD = 2.3,  $n = 43$ .

**27**: XIAP IP  $EC_{50} = 2.8$  nM, SD = 1.5,  $n = 5$ .

**Cellular cIAP1 Antagonism Assay.** MDA-MB-231 cells were plated out into 96-well plates and left overnight at 37 °C to recover. Compounds were added to duplicate wells in 0.1% DMSO for 2 h at 37 °C. Cells were lysed in 50  $\mu$ L of lysis buffer (1% Triton X-100 in 20 mM Tris.Cl (pH 7.6), 150 mM NaCl, including protease inhibitors (Roche Diagnostics Ltd., Burgess Hill, UK) for 20 min rocking at room temperature. Streptavidin-coated high-bind MSD plates (Meso Scale Discovery, Gaithersburg, USA) were coated with biotinylated anti-cIAP1 antibody (R&D Systems, Abingdon, UK) and then blocked with 3% BSA in TBST (20 mM Tris.Cl (pH 7.6), 150 mM NaCl, 0.1% Tween-20). Cell lysate was added to the 96-well anti-cIAP1 coated MSD plate and placed on a shaker for 2 h at room temperature. After washing three times with TBST, anti-cIAP1 antibody (R&D Systems, Abingdon, UK) which had been tagged with sulfo-tag (Meso Scale Discovery, Gaithersburg, USA) was added for 2 h at room temperature, with shaking. Plates were washed three times with TBST, and then read buffer was added, before reading the plate on a MESO QuickPlex SQ 120 (Meso Scale Discovery, Gaithersburg, USA). The data reported in the paper are the result of two duplicates. Compounds **2**, **5**, and **27** were tested multiple times in independent experiments and statistical limits are calculated for those compounds:

**2**: cIAP1 degradation  $EC_{50} = 0.40$  nM, SD = 0.13,  $n = 7$ .

**5**: cIAP1 degradation  $EC_{50} = 0.32$  nM, SD = 0.45,  $n = 30$ .

**27**: cIAP1 degradation  $EC_{50} = 0.22$  nM, SD = 0.21,  $n = 7$ .

**hERG Inhibition.**  $IC_{50}$  and % inhibition data were determined in the population patch clamp (PPC) assay conducted by Millipore (now Eurofins Panlabs, St. Charles, MO, USA).

**Population Patch Clamp Assay Protocol.** Inhibition of the hERG channel was measured by automated patch clamp assay in CHO K1 cells, stably transfected with the hERG ion channel. PPC measurements were performed using an IonWorks Quattro instrument (Molecular Devices Corporation, Union City, CA) using a 384 well PatchPlate (Molecular Devices Corporation) with 64 apertures per well. Each concentration of test compound was tested in duplicate wells. Amphotericin B was used to obtain electrical access to the cell interior at a final concentration of 200  $\mu$ g/mL. Human ether-à-gogo related gene (hERG) currents were measured with a prepulse to +40 mV (2 s) from the holding potential of –80 mV, followed by a step to –50 mV (2 s) to elicit the deactivating tail currents, before returning to the holding potential for 1 s. Compounds were incubated for 600 s between the pre- and postcompound reads. The external recording solution used was 130 mM Na gluconate, 20 mM NaCl, 4 mM KCl, 1 mM  $MgCl_2$ , 1.8 mM  $CaCl_2$ , 10 mM Hepes, 5 mM glucose, pH to 7.3 with NaOH. All data were filtered for seal quality, seal drop, and current amplitude. The maximum current amplitude of the third pulse tail current was calculated before (Pre) and after (Post) compound addition and the amount of block assessed by dividing the Postcompound current amplitude by the Precompound current amplitude.

**CYP Phenotyping.** Test compounds were incubated in duplicate at 1  $\mu$ M in human supersomes expressing CYP3A4 at 37 °C for 40 min at protein concentration of 20 pmol/mL, in the presence of NADPH. Positive control reference compounds (midazolam, bufuralol, diclofenac, ethoxyresorufin, efavirenz, omeprazole) were included. Negative control incubations, in the absence of NADPH, were performed. Incubations were sampled (50  $\mu$ L) at 0, 5, 10, 20, and 40 min, except for the negative controls which were sampled at 0 and 40 min.

**Metabolite Identification.** Hepatocyte suspensions with pooled cryopreserved hepatocytes at cell densities of 0.5 million cells/mL for male SD rat, male cynomolgus NHP, and mixed gender human and 0.25 million cells/mL for male CD1 mouse, were performed on compound **5** (10  $\mu$ M) at 37 °C. Incubations were sampled (100  $\mu$ L) at 0, 10, 20, 45, and 90 min. Hepatocyte samples were full scanned over a range from  $m/z$  50–1000 using LC/MS in positive ionization mode. Potential metabolite peaks were identified by comparison with negative control samples and confirmed by MS/MS fragmentation pattern scans compared to that of parent compound.

**In Vitro Permeability.** Permeability of **5** was assessed using the CacoReady system (ReadyCell, Barcelona, Spain). **5** and control compounds (propranolol, antipyrine, vinblastine) were incubated at a final concentration of 10  $\mu$ M in duplicate to either the apical (180  $\mu$ L) of the monolayer to measure apical to basolateral transport ( $A > B$ ) across the cell barrier or to the basolateral side (750  $\mu$ L) to measure the basolateral to apical transport ( $B > A$ ). For  $A > B$  spiking, **5** and control compounds were diluted from 10 mM DMSO stocks to 10  $\mu$ M in HBSS buffer with 100 mM  $CaCl_2 \cdot 2H_2O$ , 50 mM  $MgCl_2 \cdot 5H_2O$  and 0.5 mg/mL lucifer yellow made to volume with sterile water (lucifer yellow was used to determine the integrity of the Caco-2 monolayer). For  $B > A$  compound spiking, **5** and control compounds were prepared as for the  $A > B$  solutions without the addition of lucifer yellow. **5** and control compounds were incubated for 1 h at 37 °C in a highly humidified atmosphere of 95% air and 5%  $CO_2$ .

**Animal Husbandry and Handling.** Rodent studies were performed according to the Animal (Scientific Procedures) Act (1986) law. Mouse studies were performed with mice allowed access to food and water *ad libitum*. Rat studies were performed by Pharmaron (Rushden, UK). NHP studies were performed at WuXi AppTec (Suzhou, China) in accordance with the Wuxi IACUC standard animal procedures along with the IACUC guidelines that are in compliance with the Animal Welfare Act, the Guide for the Care and Use of Laboratory Animals, the Office of Laboratory Animal Welfare (OLAW) and following local ethical reviews. NHPs were housed individually in stainless steel mesh cages in a controlled environment (temperature 18 to 29 °C, relative humidity 30 to 70%) and fed twice daily.

**In Vivo Pharmacokinetic Studies.** For intravenous administrations, test compounds were formulated in 100% saline for all species. For oral administrations test compounds were formulated either in 100% water for mice, 0.5% methocel (aqueous) for rats, or 100% saline for NHPs. In rodent species, intravenous dosing was administered via the lateral tail vein at dose volumes of 1–5 mL/kg. In NHPs, test compounds were administered intravenously as a slow injection via the cephalic vein at a dose volume of 1 mL/kg. For all species, test compounds were administered orally by nasogastric gavage at dose volumes of 2–10 mL/kg. All doses were calculated as freebase equivalent per kg of bodyweight. Pharmacokinetic studies were performed in male Balb/c mice, obtained from Harlan Laboratories Inc. (Shardlow, UK), male SD rats (Pharmaron, Rushden, UK) and male cynomolgus NHPs (WuXi AppTec, Suzhou, China). Following dosing in mice, blood samples (0.2 mL) were drawn in tubes containing potassium EDTA, via either saphenous vein bleeding or cardiac puncture at various time points over 30 h using sparse sampling ( $n = 3$  per time point), prior to centrifugation (2000 g at 4 °C, 10 min). The resultant plasma was separated from the erythrocyte pellets for analysis and stored at –20 °C. In rat, blood samples (0.3 mL) were serially sampled in parallel ( $n = 3$  per route) over 24 h via the lateral tail vein and collected into EDTA containing tubes. Terminal samples were collected via cardiac puncture and centrifuged (10 000 g at 4 °C, 2 min) and the resultant plasma stored at –20 °C. Following dosing in NHPs (crossover design,  $n = 3$ ), blood samples (5 mL) were drawn in tubes containing potassium EDTA at scheduled time points over 24 h and centrifuged (3000 g at 2–8 °C, 10 min). The resultant plasma was stored at –70 °C. Noncompartmental pharmacokinetic (PK) analyses were performed using Phoenix 6.3.0.395 (Certara USA, Inc.) software. Calculated parameters included clearance, volume of distribution ( $V_{ss}$ ), time of maximum observed concentration ( $T_{max}$ ), maximum concentration ( $C_{max}$ ), terminal half-life, area under the curve (AUC) from the time of dosing to the last measurable concentration ( $AUC_{last}$ ) and extrapolated to infinity ( $AUC_{0-\infty}$ ). Noncompartmental PK fitting to sparse sampling data allowed the calculation of standard errors on  $AUC_{last}$  and  $C_{max}$  for mouse PK studies. For all other studies where a full-time profile was available noncompartmental PK fitting was applied to each individual animal (rat and NHP).

**Bioanalysis.** All in vitro and in vivo samples were extracted by protein precipitation with acetonitrile containing internal standard (1:3 v/v). For quantitative studies, calibration standards and quality controls were prepared in blank matrix and extracted under the same conditions. All samples were centrifuged at 3700 rpm at 4 °C for 20 min. Test compound bioanalysis of all in vitro and in vivo samples was performed using high performance liquid chromatography mass spectrometry with either a Quattro Ultima (Waters, UK) tandem mass spectrometer coupled to a CTC HTS PAL autosampler (CTC Analytics AG, Switzerland) and Acquity UHPLC pump (Waters, UK) or a Qtof 6150 time-of-flight mass spectrometer coupled to a 1200 UHPLC pump (Agilent, UK). Test compound and the internal standard were ionized using positive mode (ESI+) electrospray ionization. Analytes were detected using full scan or multiple reaction monitoring (MRM). Compounds typically ran on a gradient HPLC method over 5 min with a 0.1% formic acid and acetonitrile mobile phase at a flow rate of 0.5 mL/min. Separation was typically achieved using an Acquity HSS T3 1.8  $\mu$ M 50  $\times$  2.1 mm column maintained at 40 °C.

**Xenograft Studies.** MDA-MB-231 xenografts were prepared by subcutaneously injecting  $5 \times 10^6$  cells, suspended in 100  $\mu$ L of serum-free medium, into the right hind flank of male severe combined immunodeficient (SCID, BALB/cJHansHsd-Prkdcscid) mice. Tumors were measured using digital calipers and volumes calculated by applying the formula for ellipsoid. For tumor growth inhibition studies, tumor-bearing animals were randomized into groups of 7 to 8 with the average tumor volume of 100 mm<sup>3</sup> (approximately 30 days after MDA-MB-231 cell injection). Mice were randomized and compound 27 oral treatment started on Day 1. Drug-treated animals received 27 at 16 mg/kg (free base equivalent, L-lactate salt dissolved in water) and 20 mg/kg (free base equivalent, hydrochloride salt

dissolved in water then adjusted to pH 5.5 with sodium hydroxide). Control animals received water. During the treatment period, tumors were measured at least twice a week and the effect on body weight recorded daily where possible. Statistical analyses were performed using GraphPad Prism version 6. The effects of treatments were compared using one-way ANOVA and two-way ANOVA with Dunnett's multiple comparisons test against vehicle control. Differences were deemed statistically significant when  $P < 0.05$ .

**Analysis of Tumor Sample Pharmacodynamic Markers.** Xenograft tumor lysates were prepared by grinding the frozen tissue to a fine powder with a mortar/pestle under liquid nitrogen, and then adding ice-cold lysis buffer (1% Triton X-100, 150 mM NaCl, 20 mM Tris-HCl pH 7.5, plus protease inhibitors (Roche, Burgess Hill, UK), 50 mM NaF and 1 mM Na<sub>3</sub>VO<sub>4</sub>), to the ground-up tumor powder. Samples were vortexed and left on ice for 30 min. Lysates were cleared by centrifugation and samples of the supernatant removed for protein determination by BCA assay (Pierce). Meso Scale Discovery (MSD) plate-based assays were used to quantify levels of cIAP1 (cIAP1 antagonism) or levels of SMAC binding to XIAP (XIAP antagonism) in MDA-MB-231 tumor lysates as described previously.<sup>18,19</sup>

**Pharmacokinetic Analysis.** Compound levels in plasma and tumor samples were measured and pharmacokinetic parameters calculated as described previously with the exception of sample bioanalysis which was undertaken using reverse-phase liquid chromatography–mass spectrometry (MS), using a Qtrap 4000 MS (AB Sciex, UK), coupled to an Agilent 1200 HPLC system (Agilent, UK) or a Quattro Premier MS coupled to an Acquity UPLC system (Waters, UK).<sup>18</sup>

## ■ ASSOCIATED CONTENT

### 📄 Supporting Information

The Supporting Information is available free of charge on the ACS Publications website at DOI: 10.1021/acs.jmedchem.8b00900.

NMR solution conformation studies on 12; protein production for bioassay and crystallography; HCT116 negative control cell line proliferation data; cross-species in vitro intrinsic clearance values for compound 5; synthesis of compounds 7–26, NMR and LCMS plots for compound 27 (PDF)

Molecular formula strings (CSV)

### Accession Codes

Coordinates for XIAP-BIR3 complexes with compounds 12 and 21 have been deposited in the Protein Data Bank (PDB) under accession codes 6h6r and 6h6q, respectively.

## ■ AUTHOR INFORMATION

### Corresponding Author

\*Phone: +44 1223 226247. Fax: +44 1223 226201. E-mail: [chris.johnson@astx.com](mailto:chris.johnson@astx.com).

### ORCID

Christopher N. Johnson: 0000-0001-8618-9729

### Notes

The authors declare no competing financial interest.

## ■ ACKNOWLEDGMENTS

We acknowledge valuable scientific discussions with colleagues, including Tom Heightman, Chris Murray, and David Rees. The authors also thank Stuart Whibley for provision of high resolution mass spectrometry data, and Anne Cleasby for crystallographic support.

## ■ ABBREVIATIONS USED

BIR, baculovirus IAP repeat; ChrlogD, chromatographic LogD; cIAP, cellular inhibitor of apoptosis protein; CYP, cytochrome P450; DMF, *N,N*-dimethylformamide; Dmob, 2,4-dimethoxybenzyl; EDC, (3-[[[(ethylimino)methylidene]-amino]propyl]dimethylamine hydrochloride; FADD, Fas-associated protein with death domain; hERG, human ether-à-go-go related gene ( $I_{Kr}$  potassium channel); HOAT, 1-hydroxy-7-azabenzotriazole; IAP, inhibitor of apoptosis protein; IP, immunoprecipitation; MPC, manual patch clamp; NHP, nonhuman primate; NT, not tested; PPC, population patch clamp; RING, really interesting new gene; RIPK1, receptor-interacting serine/threonine-protein kinase 1; RT, room temperature; SMAC, second mitochondria derived activator of caspases; THF, tetrahydrofuran; TFA, trifluoroacetic acid; TNF, tumor necrosis factor; XIAP, X-linked inhibitor of apoptosis protein.

## ■ REFERENCES

- (1) Hanahan, D.; Weinberg, R. A. Hallmarks of cancer: The next generation. *Cell* **2011**, *144* (5), 646–674.
- (2) Fulda, S.; Vucic, D. Targeting IAP proteins for therapeutic intervention in cancer. *Nat. Rev. Drug Discovery* **2012**, *11* (2), 109–124.
- (3) Dubrez, L.; Berthelet, J.; Glorian, V. IAP proteins as targets for drug development in oncology. *Oncotargets Ther.* **2013**, *9*, 1285–1304.
- (4) Bai, L.; Smith, D. C.; Wang, S. Small-molecule SMAC mimetics as new cancer therapeutics. *Pharmacol. Ther.* **2014**, *144* (1), 82–95.
- (5) Hunter, A. M.; LaCasse, E. C.; Korneluk, R. G. The inhibitors of apoptosis (IAPs) as cancer targets. *Apoptosis* **2007**, *12* (9), 1543–1568.
- (6) Deveraux, Q. L.; Reed, J. C. IAP family proteins—suppressors of apoptosis. *Genes Dev.* **1999**, *13* (3), 239–252.
- (7) Vaux, D. L.; Silke, J. IAPs, rings and ubiquitylation. *Nat. Rev. Mol. Cell Biol.* **2005**, *6* (4), 287–297.
- (8) Eckelman, B. P.; Salvesen, G. S.; Scott, F. L. Human inhibitor of apoptosis proteins: Why XIAP is the black sheep of the family. *EMBO Rep.* **2006**, *7* (10), 988–994.
- (9) Du, C.; Fang, M.; Li, Y.; Li, L.; Wang, X. SMAC, a mitochondrial protein that promotes cytochrome c-dependent caspase activation by eliminating IAP inhibition. *Cell* **2000**, *102* (1), 33–42.
- (10) Feltham, R.; Bettjeman, B.; Budhidarmo, R.; Mace, P. D.; Shirley, S.; Condon, S. M.; Chunduru, S. K.; McKinlay, M. A.; Vaux, D. L.; Silke, J.; Day, C. L. SMAC mimetics activate the E3 ligase activity of cIAP1 protein by promoting ring domain dimerization. *J. Biol. Chem.* **2011**, *286* (19), 17015–17028.
- (11) Petersen, S. L.; Wang, L.; Yalcin-Chin, A.; Li, L.; Peyton, M.; Minna, J.; Harran, P.; Wang, X. Autocrine TNF $\alpha$  signaling renders human cancer cells susceptible to SMAC-mimetic-induced apoptosis. *Cancer Cell* **2007**, *12* (5), 445–456.
- (12) Obexer, P.; Ausserlechner, M. J. X-linked inhibitor of apoptosis protein - a critical death resistance regulator and therapeutic target for personalized cancer therapy. *Front. Oncol.* **2014**, *4*, 197.
- (13) Cai, Q.; Sun, H.; Peng, Y.; Lu, J.; Nikolovska-Coleska, Z.; McEachern, D.; Liu, L.; Qiu, S.; Yang, C. Y.; Miller, R.; Yi, H.; Zhang, T.; Sun, D.; Kang, S.; Guo, M.; Leopold, L.; Yang, D.; Wang, S. A potent and orally active antagonist (SM-406/AT-406) of multiple inhibitor of apoptosis proteins (IAPs) in clinical development for cancer treatment. *J. Med. Chem.* **2011**, *54* (8), 2714–2726.
- (14) Condon, S. M.; Mitsunuchi, Y.; Deng, Y.; LaPorte, M. G.; Rippin, S. R.; Haimowitz, T.; Alexander, M. D.; Kumar, P. T.; Hendi, M. S.; Lee, Y. H.; Benetatos, C. A.; Yu, G.; Kapoor, G. S.; Neiman, E.; Seipel, M. E.; Burns, J. M.; Graham, M. A.; McKinlay, M. A.; Li, X.; Wang, J.; Shi, Y.; Feltham, R.; Bettjeman, B.; Cumming, M. H.; Vince, J. E.; Khan, N.; Silke, J.; Day, C. L.; Chunduru, S. K. Birinapant, a SMAC-mimetic with improved tolerability for the treatment of solid tumors and hematological malignancies. *J. Med. Chem.* **2014**, *57* (9), 3666–3677.
- (15) Flygare, J. A.; Beresini, M.; Budha, N.; Chan, H.; Chan, I. T.; Cheeti, S.; Cohen, F.; Deshayes, K.; Doerner, K.; Eckhardt, S. G.; Elliott, L. O.; Feng, B.; Franklin, M. C.; Reisner, S. F.; Gazzard, L.; Halladay, J.; Hymowitz, S. G.; La, H.; LoRusso, P.; Maurer, B.; Murray, L.; Plise, E.; Quan, C.; Stephan, J. P.; Young, S. G.; Tom, J.; Tsui, V.; Um, J.; Varfolomeev, E.; Vucic, D.; Wagner, A. J.; Wallweber, H. J.; Wang, L.; Ware, J.; Wen, Z.; Wong, H.; Wong, J. M.; Wong, M.; Wong, S.; Yu, R.; Zobel, K.; Fairbrother, W. J. Discovery of a potent small-molecule antagonist of inhibitor of apoptosis (IAP) proteins and clinical candidate for the treatment of cancer (GDC-0152). *J. Med. Chem.* **2012**, *55* (9), 4101–4113.
- (16) Hennessy, E. J.; Adam, A.; Aquila, B. M.; Castriotta, L. M.; Cook, D.; Hattersley, M.; Hird, A. W.; Huntington, C.; Kamhi, V. M.; Laing, N. M.; Li, D.; MacIntyre, T.; Omer, C. A.; Oza, V.; Patterson, T.; Repik, G.; Rooney, M. T.; Saeh, J. C.; Sha, L.; Vasbinder, M. M.; Wang, H.; Whitston, D. Discovery of a novel class of dimeric smac mimetics as potent IAP antagonists resulting in a clinical candidate for the treatment of cancer (AZD5582). *J. Med. Chem.* **2013**, *56* (24), 9897–9919.
- (17) Chessari, G.; Buck, I. M.; Day, J. E.; Day, P. J.; Iqbal, A.; Johnson, C. N.; Lewis, E. J.; Martins, V.; Miller, D.; Reader, M.; Rees, D. C.; Rich, S. J.; Tamanini, E.; Vitorino, M.; Ward, G. A.; Williams, P. A.; Williams, G.; Wilsher, N. E.; Woolford, A. J. Fragment-based drug discovery targeting inhibitor of apoptosis proteins: Discovery of a non-alanine lead series with dual activity against cIAP1 and XIAP. *J. Med. Chem.* **2015**, *58* (16), 6574–6588.
- (18) Tamanini, E.; Buck, I. M.; Chessari, G.; Chiarparin, E.; Day, J. E. H.; Frederickson, M.; Griffiths-Jones, C. M.; Hearn, K.; Heightman, T. D.; Iqbal, A.; Johnson, C. N.; Lewis, E. J.; Martins, V.; Peakman, T.; Reader, M.; Rich, S. J.; Ward, G. A.; Williams, P. A.; Wilsher, N. E. Discovery of a potent nonpeptidomimetic, small-molecule antagonist of cellular inhibitor of apoptosis protein 1 (cIAP1) and x-linked inhibitor of apoptosis protein (XIAP). *J. Med. Chem.* **2017**, *60* (11), 4611–4625.
- (19) Ward, G. A.; Lewis, E. J.; Ahn, J. S.; Johnson, C. N.; Lyons, J. F.; Martins, V.; Munck, J. M.; Rich, S. J.; Smyth, T.; Thompson, N. T.; Williams, P. A.; Wilsher, N. E.; Wallis, N. G.; Chessari, G. ASTX660, a novel non-peptidomimetic antagonist of cIAP1/2 and XIAP, potently induces TNF $\alpha$ -dependent apoptosis in cancer cell lines and inhibits tumor growth. *Mol. Cancer Ther.* **2018**, *17* (7), 1381–1391.
- (20) Erickson, R. I.; Tarrant, J.; Cain, G.; Lewin-Koh, S. C.; Dybdal, N.; Wong, H.; Blackwood, E.; West, K.; Steigerwalt, R.; Mamounas, M.; Flygare, J. A.; Amemiya, K.; Dambach, D.; Fairbrother, W. J.; Diaz, D. Toxicity profile of small-molecule IAP antagonist GDC-0152 is linked to TNF- $\alpha$  pharmacology. *Toxicol. Sci.* **2013**, *131* (1), 247–258.
- (21) Komura, H.; Iwaki, M. In vitro and in vivo small intestinal metabolism of CYP3A and UGT substrates in preclinical animals species and humans: Species differences. *Drug Metab. Rev.* **2011**, *43* (4), 476–498.
- (22) Guo, L.; Guthrie, H. Automated electrophysiology in the preclinical evaluation of drugs for potential QT prolongation. *J. Pharmacol. Toxicol. Methods* **2005**, *52* (1), 123–135.
- (23) Aronov, A. M.; Goldman, B. B. A model for identifying hERG K $^+$  channel blockers. *Bioorg. Med. Chem.* **2004**, *12* (9), 2307–2315.
- (24) Waring, M. J. Lipophilicity in drug discovery. *Expert Opin. Drug Discovery* **2010**, *5* (3), 235–248.
- (25) Day, J. E. H.; Frederickson, M.; Hogg, C.; Johnson, C. N.; Meek, A.; Northern, J.; Reader, M.; Reid, G. The synthesis of 3,3-dimethyl aza- and diazaindolines using a palladium-catalysed intramolecular reductive cyclisation. *Synlett* **2015**, *26* (18), 2570–2574.
- (26) Wiggins, J. M. A convenient procedure for the reduction of diarylmethanols with dichlorodimethylsilane/sodium iodide. *Synth. Commun.* **1988**, *18* (7), 741–749.

(27) Nociari, M. M.; Shalev, A.; Benias, P.; Russo, C. A novel one-step, highly sensitive fluorometric assay to evaluate cell-mediated cytotoxicity. *J. Immunol. Methods* **1998**, *213* (2), 157–167.